Connectome of a human foveal retina

Yeon Jin Kim[1], Orin Packer[1], Thomas Macrina[2], Andreas Pollreisz[3], Christine A. Curcio[4], Kisuk Lee[2], Nico Kemnitz[2], Dodam Ih[2], Tri Nguyen[2], Ran Lu[2], Sergiy Popovych[2], Akhilesh Halageri[2], J. Alexander Bae[2], Joe Strout[2], Stephan Gerhard[5], Robert G. Smith[6], Paul R. Martin[7], Ulrike Grünert[7], Dennis M. Dacey[1,8,*]

[1]Department of Neurobiology & Biophysics, University of Washington, Seattle, WA, 98195

[2]Zetta AI LLC, Sherrill, NY, USA

[3]Department of Ophthalmology, Medical University of Vienna, Vienna, Austria

[4]Department of Ophthalmology and Vision Sciences, University of Alabama at Birmingham, Alabama 35294

[5]Aware LLC, Rappenstrasse 19, 8307 Effretikon, Switzerland

[6]Department of Neuroscience, University of Pennsylvania, Philadelphia, PA 19104

[7]The University of Sydney, Save Sight Institute and Discipline of Ophthalmology, Faculty of Medicine and Health, Sydney, NSW, 2000, Australia

[8]Washington National Primate Research Center, Seattle, WA 98195

*Corresponding author: Dennis M. Dacey (dmd@uw.edu)

This file includes: [5059 / 5000 words]

Main Text (Main text pages: 19, Total pages: 62)

Figures 1 to 10

Supplementary Information

Abstract

The foveal retina is a primate specialization which presents a feasible site for obtaining a complete connectome of a human CNS structure. In the fovea, cells and circuits are miniaturized and compressed to densely sample the visual image at high resolution, initiating form, color, and motion perception. Here we present a sample of human foveal retina analyzed by deep learning-based segmentation of all cells and synaptic connections. Cells in the volume are provisionally classified into 51 morphological types. We discovered synaptic pathways that are absent in non-human primates that may play a role in human color vision. We also demonstrate a biophysical model based on electrical synapses among short-, middle-, and long-wavelength sensitive cone photoreceptors. Segmentation of the ganglion cells, the output cells of the retina, suggests only 11 visual pathways, with 5 high-density pathways accounting for over 95% of the foveal output to the brain; this number is substantially lower than the 40+ types observed in mouse retina. The connectomic resource presented here reveals distinct features of a human neural system and highlights the potential for deep learning-based computational methods to advance understanding of the human brain.

The vertebrate retina is an accessible central nervous system (CNS) outpost where the visual process begins. It has long been appreciated for its great complexity[1] and for linking neural structure to visual function[2, 3, 4]. The retina was an early focus of synaptic-level connectomic reconstruction[5, 6, 7, 8, 9, 10], and more recently, retinal cell populations have been linked to their molecular profiles[11, 12, 13, 14] and the genetics of human disease[13, 15]. Yet even for this intensively studied neural system, we lack a full wiring diagram that could explain how vision—one of our most fundamental senses—is initiated.

The recent achievement of a complete connectome of the brain of the fruit fly, *Drosophila melanogaster*[16, 17], and application of connectomic methods to mm-scale volumes of mouse and human neocortex[18, 19, 20, 21], have made the connectome of a larger mammalian brain a conceivable goal[18, 19, 22, 23]. In the present study, we take advantage of the distinctive neural architecture of the foveal retina to provide a first draft connectome of this critical locus in the human CNS.

The fovea is a specialized central region in the retina of humans and other day-active primates where neural circuits are spatially compressed to facilitate high-resolution form, color and motion perception. At barely 1 mm wide, the fovea encodes only a few degrees of visual space, but its representation is magnified 100-fold across the surface of primary visual cortex[24, 25, 26, 27, 28]. Accordingly, the fovea is essential for normal vision, and failure of foveal function is a hallmark of devastating blinding retinal diseases.

From a signal-processing viewpoint, the fovea is an input-to-output sensory structure, where light transduction by photoreceptors is processed by diverse neural cell types across two narrow cell and synaptic layers. Here we provide a catalog of human foveal cells and their synaptic assignments to distinct functional circuits. We use this dataset to directly address the long-standing question of the number and identity of visual pathways that link the fovea to the brain. We find that only five visual pathways account for over 95% of foveal output to the

human brain: a striking reduction compared to non-primate mammals[29, 30, 31] and non-human primates[32, 33]. In addition, we observed unexpected differences in synaptic connections compared to non-human primates and provide evidence that neural coding for trichromatic color vision begins with circuitry that is uniquely human.

Results

Acquisition of the foveal volume. Our goal was to obtain complete retinal circuitry near the peak of cone density (peak of visual acuity)[34, 35]. This is a difficult task because (among other reasons) foveal cones feed inner retinal circuits via very long axons (Henle fibers, Fig. 1a-1c)[36]. Our data sample was therefore centered at 500 µm retinal eccentricity, where cone axon length averages 300-400 µm[37, 38]; this location corresponds to cones located ~100-200 µm from the center of the foveal pit (~0.5-1 deg). We cut 3028 vertical sections at 50 nm thickness through a depth of ~150 µm and imaged an area 180 µm tall x 180 µm wide at 5 nm resolution (voxel size, 5 x 5 x 50 nm^3), extending from the Henle fiber layer (outer retina) to the nerve fiber layer (inner retina) (Fig. 1d). Advanced computational methods (convolutional neural networks)[39, 40] were used to align the images, detect membrane boundaries, segment neurons, glia, blood vessels, conventional (inhibitory) and ribbon (excitatory) synapses, and predict synaptic relationships in the outer and inner synaptic layers (Fig. 1d-1k; see Methods for procedures). We named this volume HFseg1 (Human Fovea, segmented 1). All annotated cell types and the draft catalog of synaptic connections are available for exploration using search tools in an openly accessible form (https://neuromaps.app/datasets, see Supplementary Table 3) which utilizes the Neuroglancer browser and CAVE infrastructure. In addition, we created a second site, accessed via NeuroMaps, that facilitates proofreading of cells and synapses by the user community.

Cell populations

To derive and understand any connectome, the identity and layout of all cell types must first be clearly understood. Here, we took advantage of the detailed anatomical picture of foveal cell types[41, 42] that has been linked to transcriptomically defined cell clusters in human and non-human primate retina[12, 13, 43]. Moreover, for many cell populations the presence of orderly spatial arrays could be used to estimate relative density. We were therefore able to use the

98 original segmentation followed by proofreading of cell morphology (~40,000 edits to date) to
99 annotate and classify all cells and to assess the quality of synapse prediction (Fig. 1f-1g; see
100 Supplementary Table 1a, 3008 total cells with cell bodies within the volume; ~304,800 total
101 synapses, including those related to processes extending into or through the volume but not
102 linked to cell bodies).

103 In brief, HFseg1 contained 313 cone (pedicles) and 24 rod (spherules) synaptic terminals (rod:
104 cone = 0.07, Supplementary Table 1c, 1d). 17 cone pedicles were identified as short
105 wavelength-sensitive (S) cones (Fig. 2a)[44]. The remaining 296 cones comprised long (L) and
106 medium (M) wavelength-sensitive cones, here referred to collectively as LM cones.
107 Postsynaptic to cones, we annotated 268 horizontal cells and 912 bipolar cells (Supplementary
108 Table 1e, 1f). It was possible to distinguish the H1 and H2 horizontal cell types (Fig. 3) and
109 most of the classically recognized bipolar cell types (Fig. 4) by distinctive morphology and
110 connectivity. Some exceptions will be considered further below.

111 We annotated 293 amacrine cells, including 40 cells displaced to the ganglion cell layer (Fig. 5;
112 Supplementary Table 1g; Supplementary Fig. 8), first dividing cells by dendritic field diameter
113 into small (diameter < 100 μm; n = 189), and large-field (diameter >100 μm) groups (n = 104).
114 We divided these groups in turn into 19 types (6 small-field and 13 large-field; Supplementary
115 Table 1g) based on morphology, stratification, mosaic interactions and nuclear morphology
116 (Supplementary Figs. 3, 6, 8). Figure 5 provides a partial view of this dataset by highlighting
117 four cell types (see also Supplementary Table 3); two additional amacrine populations are
118 illustrated in Supplementary Fig. 8 and others can be viewed at the NeuroMaps site.

119 We annotated 599 ganglion cells (Fig. 6; Supplementary Table 1h). As expected, the
120 classically recognized midget GCs constitute the great majority (536 cells, ~90%)[13, 45]; these
121 cells were readily divided into outer-OFF stratifying (n = 280 cells) and inner-ON stratifying (n =
122 256) types (Fig. 6a, 6e). A second well-defined cell group, the parasol cells (26 cells, 13 inner-

123 ON cells and 13 outer-OFF cells, ~4% of total GCs), was also easily distinguished (Fig. 6b, 6f).
124 Small bistratified GCs[46], found to show blue-yellow color opponency in macaque retina[47, 48]
125 were distinguished by their broad dendritic ramification (12 cells, ~2% of total GCs; Fig. 6c, 6g)
126 and extensive synaptic input from blue cone bipolar cells (BB cells)[49]. Together, the midget,
127 parasol and small bistratified cells accounted for 95.8% of the ganglion cells in HFseg1
128 (Supplementary Table 1h). The remaining 25 ganglion cells showed relatively large dendritic
129 fields (Figs. 6d, 6h–6n) and were divided into 5 provisional groups comprising 6 types
130 (Supplementary Table 1h; Supplementary Notes) pending a more detailed analysis of their
131 synaptic connections, giving a total of 11 ganglion cell populations in this volume–this number
132 is very close to the 12 populations identified for central human retina by molecular profiling[13].

133 Finally, glial cells were readily distinguished from all neurons by their distinctive ultrastructure
134 (Supplementary Figs. 3a, 3b, 3c, 3f). The Müller cells (555 cells, Fig. 1f,1g; Supplementary
135 Table 1b) were distinguished as radial glia with cell bodies in the inner nuclear layer
136 (Supplementary Fig. 1a). A second, morphologically distinct population of glial cells in the GCL
137 was closely associated with superficial blood vessels (Supplementary Figs. 1b, 3b) and
138 identified as astrocytes[50] (32 cells, Supplementary Table 1b; Supplementary Fig. 1b). We also
139 identified 15 microglial cells (Supplementary Table 1b) with cell bodies in the IPL or GCL
140 (Supplementary Figs. 1a, 1b, 3c, 3b). The density of microglial cells was low, consistent with
141 previous measurements in the macaque monkey foveal retina[51, 52]. In the current volume, we
142 have not yet attempted to characterize blood vessel and associated pericytes, though these
143 cellular elements are also segmented and are available to annotate and further characterize.
144 More detailed information on cell type identification is provided in the supplementary
145 information (Supplementary Notes on cell type identification).

146 **Synapse detection**

147 To assess the accuracy of ribbon segmentation and synapse prediction (Fig. 1h-1k), we
148 compared deep-learning-predicted synaptic assignments to manual (ground truth)
149 assignments. We focused on the cone-to-midget bipolar cell synapse in the OPL and the
150 midget bipolar cell synapses to amacrine and ganglion cells in the IPL. For ground truth, we
151 manually annotated all midget pathway synaptic connections for three LM cones (cones 21, 22,
152 and 58; Supplementary Fig. 9; Supplementary Table 2a-2c).

153 Figure 7 shows the predicted outgoing synapses for a pair of midget bipolar cell axon
154 terminals. We calculated precision (true synapses / [true synapses + false positives]; the
155 accuracy of positive predictions) and sensitivity (true synapses / [true synapses + false
156 negatives]; the proportion of true synapses identified) for ribbons and their synapses. The
157 segmentation of ribbons showed high precision and sensitivity near 100% (precision: 93.5% ±
158 2.7%; sensitivity: 99.7% ± 0.8%, n = 6 midget bipolar cells, 370 total ribbons; Fig. 7b inset).
159 Postsynaptic partner assignment for these ribbons was also excellent (precision: 89.0% ±
160 5.4%; sensitivity: 93.7% ± 4.6%, n = 6 midget bipolar cells, 637 total synapses; Fig. 7b inset).
161 These values demonstrate the high accuracy of convolutional nets for predicting and
162 segmenting ribbon synapses.

163 In contrast to the ribbon synapses made in the IPL, ribbon synapses made by the cone pedicle
164 in the OPL are extremely complex[53, 54] (Fig. 1h, 1i). Postsynaptic processes can either
165 invaginate into the face of the pedicle or occupy a basal position at the cone pedicle up to ~800
166 nm from the sites of transmitter release[54, 55]. We mapped all cone-to-bipolar synapses at the
167 dendritic tips for a sample of six midget bipolar cells. We found high precision and sensitivity for
168 ribbon detection (n = 51 ribbons) (precision: 92.3% ± 6.7%; sensitivity: 100%, n = 3 LM cones,
169 Supplementary Fig. 2a-2c) and for the postsynaptic processes (n = 153) deriving from the
170 invaginating (IMB) and flat (FMB) midget bipolar cells (precision: 98.7% ± 1.2%; sensitivity:

171 99.7% ± 0.6%, n = 153 total synaptic connections; see Supplementary Fig. 2c right). Diffuse
172 bipolar (DB) cells, which make sparser connections with multiple cones, were also sampled (n
173 = 2, DB4 and DB2; Supplementary Fig. 2d-2f), yielding similar precision and sensitivity values.

174 For inhibitory synapses, we focused on the AII amacrine cell (Figs. 5a, 7c, 9; Supplementary
175 Table 1g) where glycinergic synapses to OFF bipolar cell axon terminals are well established[56,
176 57, 58, 59]. We manually mapped all the outgoing synapses made by two neighboring AII amacrine
177 cells and compared our ground truth data to the predicted synaptic assignments (Fig. 7c-7g).
178 The prediction captured well the synaptic output from the outer stratifying lobular appendages
179 of the AII cell to outer-OFF bipolar cells (Fig. 7d-7g). Vesicle clouds were detected with high
180 sensitivity (87.5% ± 0.7%, n = 2 AII cells; false negatives were rare; Fig. 7c inset), but relative
181 to ribbon detection, there were more false positives, thereby reducing precision (76.0% ± 8.5%,
182 n = 2 AII cells). Despite this limitation, the results show that our dataset predicts synaptic
183 connectivity with good sensitivity and precision. However, we implemented methods within the
184 Neuromaps interface to proofead all synapses for accuracy.

185 Having established the accuracy of our connectomic dataset, we examined the cell types and
186 their synaptic connections to identify features that are distinctive in human compared to non-
187 human primate. Below we highlight examples where differences are dramatic and warrant
188 further study.

189 **Modeling the connectome: S-LM cone electrical coupling alters spectral tuning.**

190 Cone pedicles contact each other by short extensions (telodendria) or by distinct pedicle-to-
191 pedicle appositions at perforations in the glial sheath surrounding cone synapses (Fig. 2b).
192 These contacts harbor gap junctions, i.e., electrical synapses that mediate a conductance
193 between cones, including L and M cones[60]. In non-human primates, L to M cone contacts are
194 abundant, but S to LM contacts are greatly reduced or absent[44, 61]. In the macaque, electrical

195 coupling was absent between LM and S cones[60], consistent with a lack of contacts between
196 these cone types[61, 62]. The crosstalk between L and M cones serves to reduce noise in the
197 light-evoked response with a small cost to spectral separation[63, 64, 65]. The lack of gap junctions
198 between LM and S cones has been interpreted as reflecting the need to keep S and LM cone
199 signals separate to build color-coding receptive fields at later stages in color processing[66, 67].

200 Unlike in the macaque, S-LM cone contacts have been reported in human retina[44, 68]. We
201 therefore mapped the full cone-cone connectome to determine whether S-LM contacts are a
202 consistent feature of the human fovea. Cone-cone contacts (n = 1141) were characterized by a
203 thick, darkly stained region defining the contact area (see Fig. 2c)[69]. We found abundant S-LM
204 cone contacts (n = 17 S cones; 5.25 ± 2.11 contacts/S-cone pedicle), indistinguishable from
205 LM-LM cone contacts (n = 296 LM cones; 6.89 ± 3.08 contacts/pedicle). We then used this
206 cone-cone connectome dataset to estimate the effect of S-LM coupling on spectral tuning in a
207 simulated cone-cone network, using known parameters for gap junction number and single
208 channel conductance values as follows. We mapped the surface area of the contacts among all
209 cones in the volume (Fig. 2a), using automated methods to generate the "contactome" between
210 cone pedicles. Detected contacts were inspected and filtered by size to remove very small and
211 likely spurious contacts. The surface area of each contact was calculated (n = 1141 contacts;
212 mean surface area 0.56 ± 0.31 μm^2). In general, contacts were large and obvious with a
213 relatively thick, darkly stained region defining the contact area (see Fig. 2c), reflecting the
214 presence of large adherens junctions at the contact site[69]. We calculated the conductance for
215 each contact based on previously measured densities for gap junctions and the conductance of
216 single gap junction channels (9 gap junctions/μm^2 at 15 pS/junction; see Methods for details).
217 We used a fixed ratio of L to M cones of ~1.7:1, randomly assigned[70], and incorporated the
218 cone-cone coupling given by our contactome (Fig. 8a). Each cone was modeled
219 compartmentally as a soma, Henle fiber-axon, and synaptic terminal (see model parameters in

220 Supplementary Table 4). Our modeled average coupling conductances were low (LM-LM cone
221 pairs, 133 pS, n = 25 cones; S-LM cone pairs, 166 pS, n = 15) by comparison with
222 conductances measured directly between LM cone pairs in the macaque (> 500 pS) or cone
223 pairs in non-primate mammalian retina (~220-320 pS)[65, 67]. Nevertheless, we found that even
224 with this conservative estimate of coupling conductance, the S-cones showed an increased
225 sensitivity to light pulses at longer wavelengths in the model (Fig. 8b). We measured the effect
226 on spectral sensitivity by simulating light responses from L, M, and S cones at 5 nm
227 wavelength intervals across the visible spectrum. The results demonstrate a broad secondary
228 elevation in sensitivity for S cones at longer wavelengths that peaks at ~550 nm (Fig. 8c-8d) in
229 the coupled cone network. These data provide evidence that S-LM cone coupling can directly
230 influence the spectral tuning of the voltage response of S cones and raise the question of how
231 this network feature affects downstream processing.

232 **Trichromatic horizontal cells**

233 A second difference in synaptic connectivity that may impact color vision occurs at the synapse
234 between cones and horizontal cells. The horizontal cell network in the outer retina generates
235 lateral negative feedback that underlies the antagonistic receptive field surround of cones,
236 bipolar cells, and ganglion cells[71]. In the macaque monkey retina, the horizontal cell-mediated
237 surround is a key element in the circuitry that initiates red-green color vision[72, 73, 74]. In the
238 peripheral retina of the macaque and marmoset, H1 cells make dense contacts with LM cones
239 but largely or completely avoid contact with S cones, whereas H2 cells show some selectivity
240 for S cones[75, 76, 77]. While foveal H2 cells in HFseg1 maintained a clear preference for
241 synapsing with S cones (Fig. 3b), we found that H1 cells also received a major input from S
242 cones, comparable to H2 cells (H1, 43% ± 16%; H2, 57% ± 16%, n = 10 S cones). By contrast,
243 H2 cells formed less than 2% of the horizontal cell contacts with LM cones (H1, 98.1% ± 0.1%;
244 H2, 1.9% ± 0.1%, n = 2 LM cones) (also Supplementary Fig. 4). Consequently, human foveal

245 H1 cells are predicted to show a trichromatic receptive field with a small S cone contribution
246 (Fig. 3; Supplementary Fig. 4). Taken together, the S-LM cone coupling and the combined S
247 and LM cone connectivity of H1 horizontal cells provide new connectomic evidence for
248 differences between human and non-human primate circuits that initiate color vision[44].

249 **Unexpected cell types and circuits in HFseg1**

250 We also found differences in both bipolar and amacrine cell circuits compared to expectations
251 from the macaque monkey, whereby some bipolar cell types were either greatly reduced or
252 absent. For example, DB-OFF bipolar cells can be divided into 4 morphological types (DB 1, 2,
253 3a and 3b) in macaque monkey[78, 79] but we were only able to distinguish three populations by
254 mosaic arrangement and stratification in the IPL that we call DB1, 2 and 3 (see Supplementary
255 Notes). Bipolar cell morphologies not previously described in primates were also present. One
256 bipolar group showed amacrine-like morphology (outer-x and inner-x, Fig. 4a, 4b) but
257 contained abundant synaptic ribbons (20 cells, Supplementary Table 1f; Supplementary Fig. 6).
258 Similar cells were discovered recently in mouse retina[11, 80] and likely correspond to the OFF-x
259 bipolar cells identified by transcriptomics of human fovea[13]. While most of these cells stratified
260 in the outer half of the IPL (outer-x cells, n = 15, Supplementary Fig. 6a-6b), five cells stratified
261 in the inner half of the IPL (inner-x cells, Supplementary Fig. 6c-6g). Another previously
262 undescribed bipolar type showed the characteristic DB cell connection to multiple cones but
263 extended axonal branches in both outer and inner IPL where it provided synaptic output to
264 outer-OFF and inner-ON ganglion cell types (see also Supplementary Fig. 7c, 7e). We refer to
265 this cell group as DBbroad (18 cells, Fig. 4a; Supplementary Fig. 7; Supplementary Table 1f).
266 The HFseg1 volume offers a unique opportunity to further understand these novel bipolar cell
267 populations.

268 For the amacrine cells, the AII type (AC2) was present at the highest density of any amacrine
269 cell population (26%, 75 cells, Figs. 5a, 5b, 7c, 9; Supplementary Table 1g). This cell type was

recognized by its well-established morphology across species[56], including humans[41, 57, 81]. A major function of AII cells is to transfer signals from rod bipolar to cone bipolar cells, serving as conduits for rod signals to ganglion cells at scotopic light levels[82]. The presence of AII amacrine cells at such a high density in the fovea, where rods are nearly absent, suggests, however, a functional switch to a primary role in photopic spatial vision. Indeed, we observed that AII cells are postsynaptic to all cone bipolar types, including IMB and FMB cells, across the full extent of the dendritic tree (Fig. 9). These data support the general view that AII cells "have a day job"[57] to provide an inhibitory pathway from ON to OFF bipolar cells under photopic conditions[82, 83, 84] while at the same time suggesting specialized synaptic alterations for the AII cells in the human fovea in relation to the midget circuit.

Visual pathway reduction: the vertical excitatory connectome

Despite its fundamental importance, the number of visual pathways linking the human fovea to the brain is still unknown. Our classification of 11 ganglion cell types suggests that several ganglion cell types observed in the monkey and human retinal periphery are absent from the human fovea. This result also stands in sharp contrast to the retina of the mouse, where ~40 GC types have been distinguished independent of retinal location[29, 30, 31]. Our classification, however, did not rule out the possibility that some ganglion cell types with somata outside HFseg1 have dendritic trees which penetrate the volume and contribute substantially to the synaptic connections of the inner retina. We therefore took a second approach to identifying the visual pathways in HFseg1 by mapping what we called the "vertical excitatory connectome".

We reasoned, as others have[85], that to generate parallel pathways to the brain, each cone photoreceptor must be locally presynaptic to each cone bipolar type (For the S cones, there is uncertainty regarding this point, due to their more specialized role in color vision[86, 87]). At the

294 next synaptic step, the combined output of all bipolar cell types should be distributed to all
295 ganglion cell types. In other words, in principle, *all visual pathways should be synaptically*
296 *linked to the output of any given cone*.

297 To test this hypothesis, we annotated the ribbons within five cones (three LM and two S) and
298 their postsynaptic bipolar cells. For each bipolar cell, all synaptic ribbons and their postsynaptic
299 GC partners were then identified (Fig. 10a-10b). Finally, we determined the relative synaptic
300 density from a given cone via its postsynaptic bipolar cells to each identified GC type (see
301 details in Supplementary Figs. 9 and 10; Supplementary Table 2).

302 We found that bipolar cells that were postsynaptic to the three LM cones provided their output
303 overwhelmingly to midget and parasol ganglion cells (Supplementary Fig. 9), accounting for
304 92.1% of the total bipolar synaptic output to ganglion cells (Fig. 10c, 10d; Supplementary Fig.
305 9; Supplementary Table 2a-2c). The remaining ~7.9% of bipolar synapses were directed to the
306 large-field ganglion cell types (LFGC1-LFGC5, Fig. 10d, 10h, and 10i-10n; Supplementary Fig.
307 9; Supplementary Table 2a-2c). Output to dendritic fragments of unidentified ganglion cells was
308 rare, accounting for only ~0.5% of the total bipolar output to ganglion cells (0.53 ± 0.76%, n = 3
309 LM cones, Supplementary Table 2a-2c). These data support the conclusion that, with the
310 possible exception of extremely large-field and low-density melanopsin-expressing ganglion
311 cells, we have accounted for all ganglion cell types present in our foveal sample.

312

313

314

315

316

317

318 **Discussion**

319 **A human foveal connectome.** Our aim was to provide a draft nanometer-scale connectome in
320 the human CNS. Compared to ongoing studies of a larger volume of human neocortex[18], our
321 foveal volume has the advantage that foveal circuitry is miniaturized and functionally complete
322 – from receptors to ganglion cell outputs. Moreover, all cell types in the HFseg1 volume are
323 identified and can be related to anatomical, physiological, and transcriptomic studies of human
324 and non-human primate retina (Supplementary Table 1).

325 **Cell type profiling.** Comparable datasets to HFseg1 exist for primate central retina where cell
326 types were clustered by gene expression profiles[12, 13, 15, 43, 88]. The HFseg1 volume permits a
327 comparison of the two approaches and suggests generally good correspondence, though with
328 some unexpected differences. For example, the ratio of H1 to H2 horizontal cell types identified
329 by transcriptomic analysis was shown in the macaque and human central retina to be ~3:1 and
330 7:1, respectively. By contrast, the H1 to H2 ratio in HFseg1 is much higher (22:1), with H1 cells
331 comprising 96% of the horizontal cells at this foveal location. Thus, the trend toward H1 cell
332 dominance in the transcriptomic dataset is evident but more extreme in HFseg1. A similar trend
333 holds for other clearly identified types: for example, midget ganglion cells make up ~90% of the
334 ganglion cell population in our sample and 86% in the transcriptomic dataset; AII amacrine
335 cells make up 26% of the amacrine cells but only 18% of the amacrines identified by
336 transcriptomic analysis. One explanation for these differences may be that our smaller sample
337 represents the cone-enriched foveal center, whereas the larger samples used for
338 transcriptomics encompassed a much larger area (~1.5 mm, central 5 degrees). Cell type-
339 specific density changes are extremely steep across this region, so that larger spatial samples
340 would average out such changes.

341 Certain cell populations previously recognized were not evident in HFseg1. For example, the
342 recent functional, anatomical, and molecular distinction made between DB3a and DB3b in the
343 macaque monkey[79, 89] and human retina[13, 38] was not apparent in HFseg1. Further, we found
344 evidence for only 19 amacrine cell types, whereas molecular profiling in human retina
345 (including the retinal periphery) has proposed 73 amacrine cell types[15]. By comparison, 63
346 amacrine clusters have been identified in mouse retina[90, 91]. These differences suggest that the
347 relationship between cells defined by gene expression and anatomical types may not always
348 be straightforward. A further implication is that the extreme increase in density of the midget
349 circuit, required for high acuity and color vision, gives rise to an attendant density increase in
350 other foveal cell types tightly linked to the midget pathway (e.g., H1 horizontal cells).

351 **The vertical excitatory connectome.** In the non-human primates, fewer than 20 ganglion cell
352 types have been defined, with transcriptomic and anatomical identification in close
353 agreement[12, 32, 33]. In the human fovea, only 12 pathways have been suggested by
354 transcriptomic analysis[13, 15]. It was nevertheless striking that in the HFseg1 dataset
355 (Supplementary Table 1h), ~96% of the ganglion cells comprised just five anatomically distinct
356 pathways: the ON and OFF midget and parasol cells, and the small bistratified cells. When we
357 manually traced the vertical connectome from a single cone to its postsynaptic bipolar and
358 ganglion cells, we found that ~92% of synaptic output targeted these same five pathways (Fig.
359 10d), confirming their dominance. Thus, a fundamental, defining feature of foveal synaptic
360 organization may be a reduction in the number of visual pathways compared to the peripheral
361 retina.

362 Over 40 distinct ganglion cell populations have been recognized in the mouse retina, with
363 molecular profiling, physiology, and anatomy in agreement[29, 30, 31]. What explains this dramatic
364 reduction in ganglion cell types from the mouse retina to the primate fovea? The difference
365 suggests that humans and mice have evolved fundamentally different solutions to analyzing

366 the visual scene. Great emphasis has been placed on the behaviorally relevant feature-
367 detection properties of diverse mouse ganglion cell types[92, 93, 94]. By contrast, in primates,
368 considerable emphasis has been placed on the dual and more general role of the midget
369 pathway in both form and color perception[74, 95, 96].

370 Recent molecular orthotype analysis shows that the midget and parasol ganglion cell types
371 are likely homologous to sustained and transient alpha cell types, respectively, in the mouse[14].
372 What differs dramatically, however, is the extremely large dendritic tree and consequent low
373 spatial density (~2% of the total ganglion cells) of the mouse ortholog of the midget ganglion
374 cell. Thus, the mouse retina sacrifices spatial resolution[97], opting instead for an expansion of
375 feature detectors that rely on trigger features linked to motor output—with mice employing
376 feature-detection strategies analogous to those described in classical studies of amphibian
377 vision[98]. In primates, the midget circuit represents an evolutionary extreme where the spatial
378 resolution afforded by tightly packed photoreceptors is preserved through private-line
379 connectivity. This high-resolution sampling is behaviorally exploited through active vision
380 strategies. Humans not only explore a visual scene by making saccadic eye movements but
381 also make small fixational eye movements (microsaccades) to extract information at peak
382 resolution[99]. These microsaccades are dynamically modulated during highly precise
383 manipulation (e.g., threading a needle)[99, 100, 101]. Thus, the incessantly mobile fovea and
384 related retinal circuits are designed for inspection, manipulation, interpretation, and
385 understanding of an object—the converse of a feature detector.

386 **The foveal connectome and human color vision.**

387 *S cone input to H1 cells.* Most psychophysically based models of human color vision assume
388 the presence of two parallel color-opponent channels: red vs green and blue vs yellow[109]. The
389 red-green pathway shows opposing L vs M cone interaction and has been associated with the
390 circuitry that feeds midget ganglion cells[102]. However, the human psychophysically defined red-

391 green pathway includes a small S cone input[103]. The locus of this critical signal pathway
392 remains unclear, with recent data from the macaque monkey implicating both the retina[110] and
393 primary visual cortex[111]. The HFseg1 connectome shows that H1 horizontal cells, a major
394 source of the surround in the midget circuit[51], likely contribute antagonistic signals from all
395 three cone types (L, M, and S) to the midget pathway. In this scenario, the human foveal
396 midget circuit would derive its center response from either an L or M cone, while the surround
397 would provide cone opponency by non-selectively contacting all three cone types[73, 104, 105], with
398 the S cones making a small contribution to the chromatic receptive field, creating L+S vs M or
399 M+S vs L opponency.

400 *S-LM cone coupling.* As a first step in deriving the foveal connectome, we determined the
401 "contactome" among the tightly packed cone synaptic pedicles. Contacts among the cone
402 types harbor gap junctions and thus form electrical synaptic connections between cones[65, 69].
403 We confirmed and extended previous observations suggesting that, in contrast to non-human
404 primates and non-primate mammals, human foveal S cones show extensive telodendritic
405 contacts with neighboring LM cones[44, 68], and these contacts are identical in form to LM-LM
406 cone contacts.

407 A network model of this connectivity showed that, as a previous model suggested[66], that mixing
408 S and LM cone signals can alter the action spectrum of the S cone light response, with
409 increased sensitivity at longer wavelengths. This result raises a functional puzzle: the prevailing
410 view is that electrical coupling serves to increase signal relative to noise by reducing the
411 uncorrelated voltage difference (i.e., the noise component) among neighboring cones and
412 thereby increase contrast sensitivity[66]. However, any mixing of S and LM cone signals would
413 detract from the separation of cone signals required for color processing, in turn raising the
414 question of why such coupling occurs in human foveal retina, whereas it is absent in both the
415 macaque and marmoset retina[44].

416 The answer may be related, at least in part, to the connectivity of H1 horizontal cells with S
417 cones noted above. Coupling among the S, L, and M cones prior to this connection may serve
418 to preserve the smaller S cone signal within the H1 cell network. This in turn may be critical for
419 the unique requirements of human color vision whereby a small S cone signal contributes
420 critically to the “red-green” chromatic channel defined psychophysically[103]. This hypothesis
421 could be tested by adding the horizontal cell connectome to the current cone-cone network and
422 testing the effects of noise and coupling on the spectral tuning of the H1 cell response and
423 ultimately its contribution to cone opponency modeled in the midget ganglion cell.

Acknowledgements

This work was supported by NIH grants EY-028282 and RF1-MH129260 to D.M.D. and NIH grant P51 OD010425 to the Washington National Primate Research Center and EY01730 to the Vision Research Core at the University of Washington. We thank Sharm Knecht for tissue preparation and managing EM data acquisition.

Author contributions

Y.J.K. and D.M.D. conceived the project. Y.J.K. and D.M.D. generated the ground truth for segmentation and synapses, performed proofreading and created annotations. R.G.S constructed and ran the computational models. Y.J.K. and D.M.D. analyzed the data and generated figures. Y.J.K., D.M.D., P.R.M., and U.G., wrote the paper and consulted on cell type annotations and figure development. C.A.C. and R.G.S., edited the paper. A.P. acquired human tissue. D.M.D., Y.J.K., C.A.C. and A.P. acquired funding. Zetta AI performed EM data alignment, segmentation, synapse detection and cone-cone contactome detection and ingested all data into the CAVE infrastructure for proofreading. S.G. developed 3D visualizations and analysis tools at NeuroMaps.app.

Declaration of interests

K.L., N.K., D.I., T.N., R.L., S.P., A.H., J.A.B., J.S. and T.M. declare financial interests in Zetta AI. S.G. is owner of Aware LLC and developed the NeuroMaps.app. The remaining authors declare no competing interests.

Figures and figure legends (10 Figures)

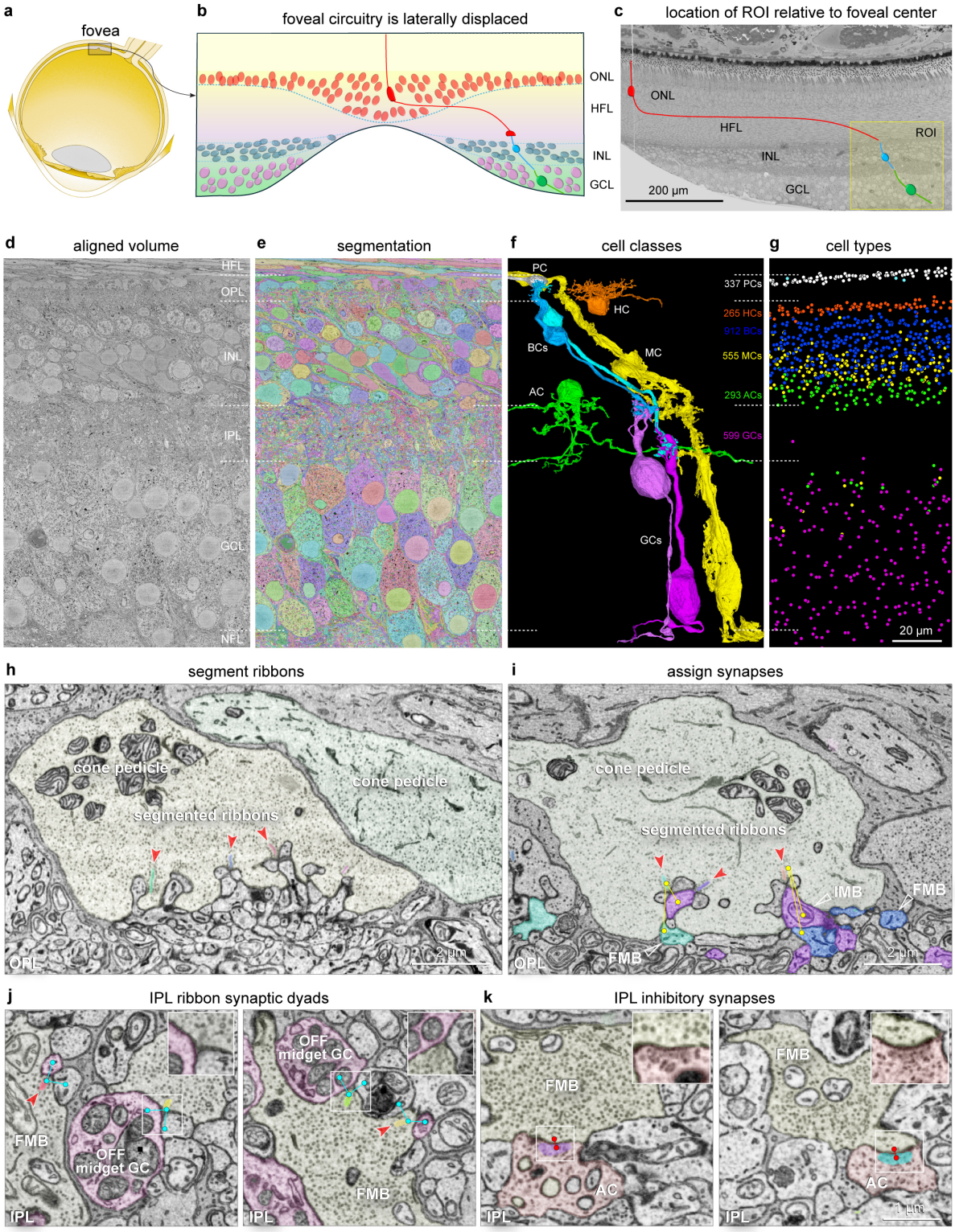

447 **Fig. 1. The HFseg1 volume**. **a.** The fovea forms a pit in the retina ~3 mm temporal to the
448 optic disc (within the inset rectangle). **b**. Schematic foveal pit showing cone (red) to bipolar
449 cell (blue) to ganglion cell (green) circuit. ONL, outer nuclear layer; HFL, Henle fiber layer;
450 INL, inner nuclear layer; GCL, ganglion cell layer. **c**. Trimmed retinal block face and ROI
451 (yellow box) in temporal retina 400-500 µm from the foveal center. **d**. Single section from the
452 imaged volume (cropped laterally) to illustrate the retinal layers; HFL; OPL, outer plexiform
453 layer; INL; IPL, inner plexiform layer; GCL and NFL, nerve fiber layer. **e**. Volume segmented
454 into membrane-bound objects. **f**. Examples of segmented cells: photoreceptor axon terminal
455 (PC, white), horizontal cell (HC, orange), ON and OFF bipolar cells (BC, light and dark blue),
456 Müller glia cell (MC, yellow), amacrine cells (AC, green), ON and OFF ganglion cells (GC,
457 dark and light violet); astrocytes and microglia not shown here. **g**. Numbers and cell soma
458 locations of the cell types shown in **f**. **h.** Three segmented ribbons (varied colors) at synaptic
459 triads (red arrowheads) in a single cone pedicle. **i.** Synaptic assignments associated with each
460 ribbon (yellow dots and lines). An IMB (inner-ON midget bipolar; violet, white open arrowhead)
461 cell makes an invaginating contact and two FMB cells (outer-OFF midget bipolar; light and
462 dark blue, white open arrowheads) make a basal contact with the cone pedicle. **j.** Examples of
463 ribbon and synapse prediction in the inner plexiform layer (IPL) for an FMB cell axon terminal
464 at two locations (left and right panels). Segmented ribbons (varied colors, red arrowheads)
465 and synaptic predictions (blue dots, lines) are shown. **k.** Inhibitory vesicle cloud segmentation
466 (varied colors) and synaptic prediction (red dots and lines) in the IPL between an amacrine
467 cell and an FMB axon terminal are shown. Insets in **j** and **k** show zoomed-view of synapses
468 indicated by white boxes.

469

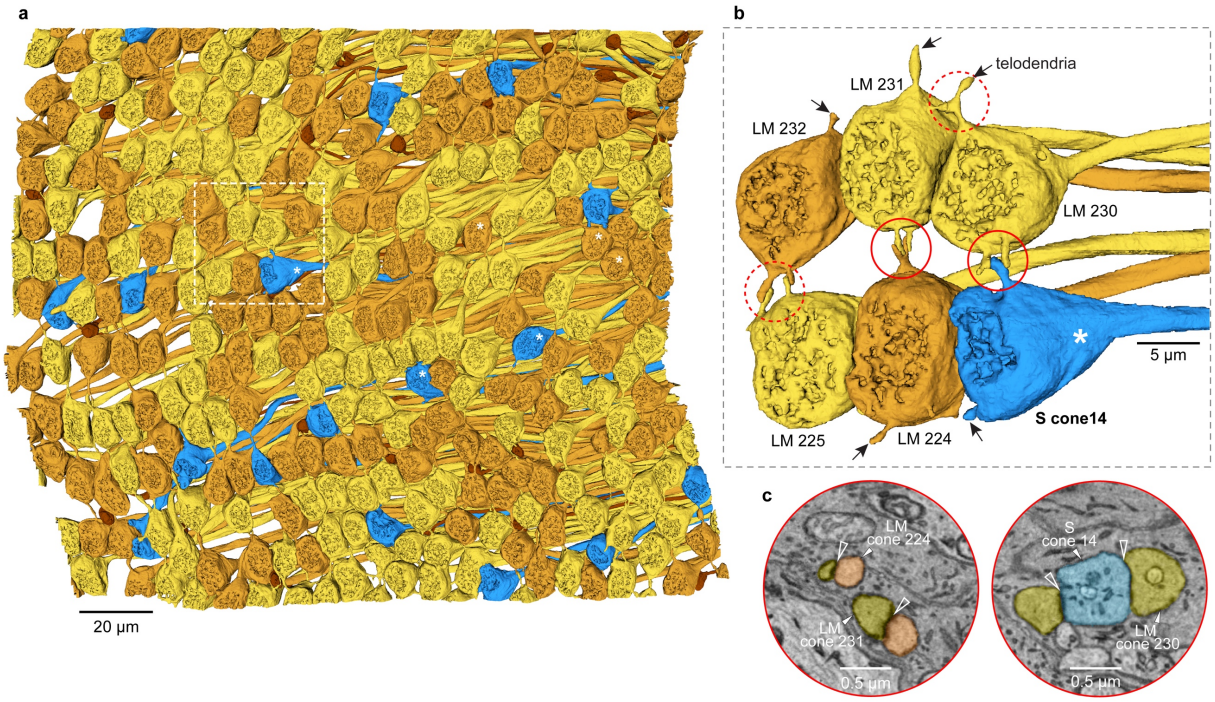

Fig. 2. Photoreceptors. a. Array of photoreceptor axon terminals (cone pedicles, rod spherules) viewed from the synaptic face of the terminals (296 LM cones, gold; 17 S cones, blue, 24 rods, brown) (see Supplementary Table 1a, 1c, 1d). Five cones marked with white asterisks were used to generate the vertical connectome analysis shown in Supplementary Figs. 9 and 10 (S cones 54 and 103; LM cones 21, 22, and 58). **b**. Six cone pedicles within the white dotted box in **a**. These pedicles contact each other via telodendria (e.g., arrows) within the circled areas. A pedicle identified as an S cone (white asterisk) contacts neighboring LM cone 230. **c**. EM micrographs showing telodendritic contacts corresponding to the two solid red circled areas in **b** (open white arrowheads). Left solid red circle shows contacts between LM cones 231 and 224, and the right solid red circle shows S cone 14 contact with LM cone 230. Cone-cone contact surface areas were calculated and used in the simulation shown in **Fig. 8**.

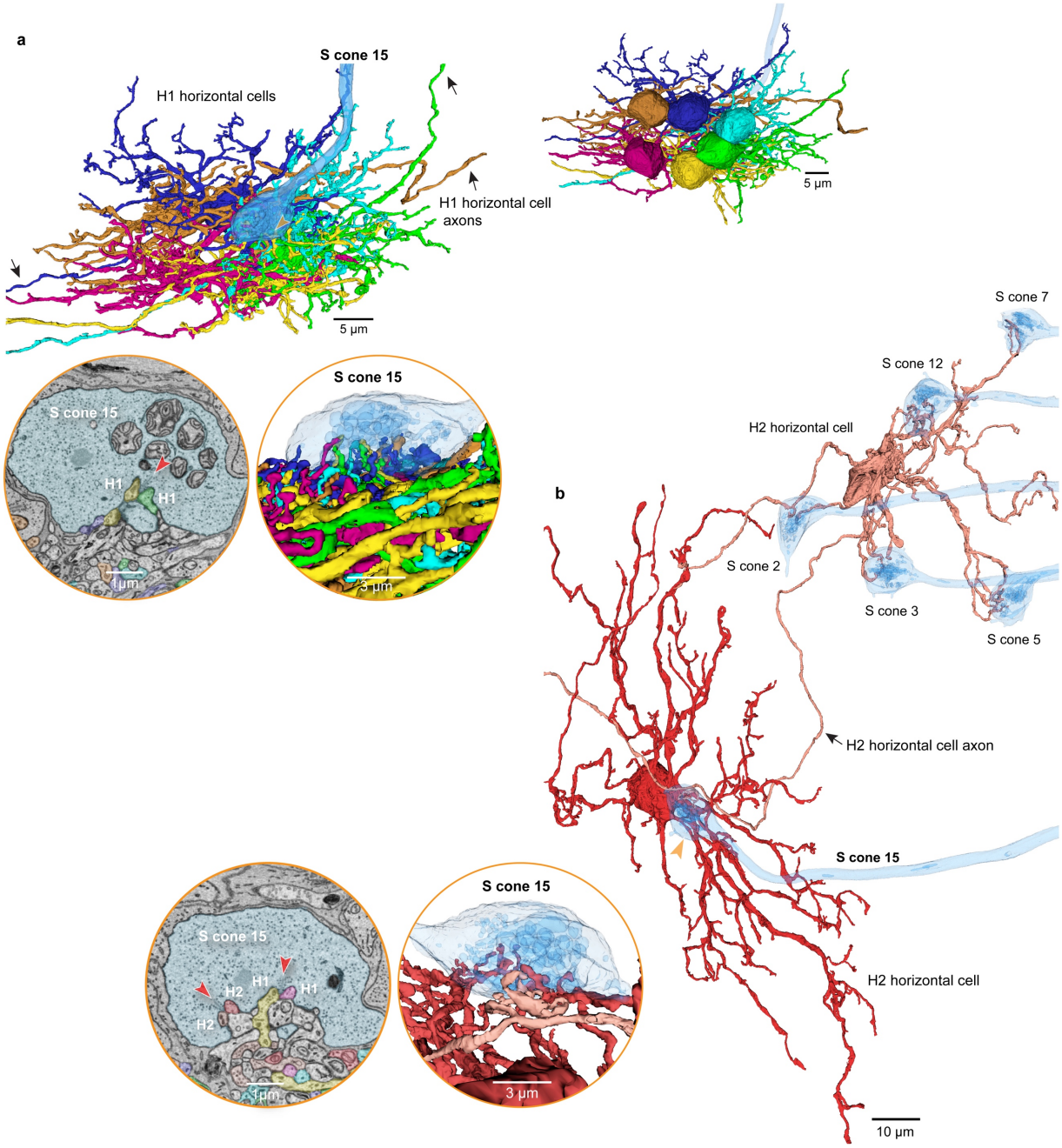

482

483 **Fig. 3. H1 and H2 horizontal cells synapse with S cones.** a. Six overlapping H1 cells are
484 shown (varied colors); each H1 cell forms lateral elements in S cone 15 (blue). The upper
485 inset is an inverted view that shows the cell bodies of the six H1 cells. Circular inset at lower
486 left shows EM view of H1 cell lateral elements at a synaptic invagination of S cone 15 (red
487 arrowhead). Circular inset at lower right shows a 3D view of S cone 15 (partial transparency)
488 contacting multiple H1 cells. H1 cells made 43% ± 16% of the total contacts with S cones (n =

489 10 S cones). **b**. Two H2 cells (tan and red) contact multiple S cones, including S cone 15.

490 Lower insets show H2 cell lateral elements at S cone 15 in single-layer EM view (left) and 3D

491 (right) view (conventions as in **a**). H2 cells made 57% ± 16% of the total contacts with S cones

492 (n = 10 S cones).

493

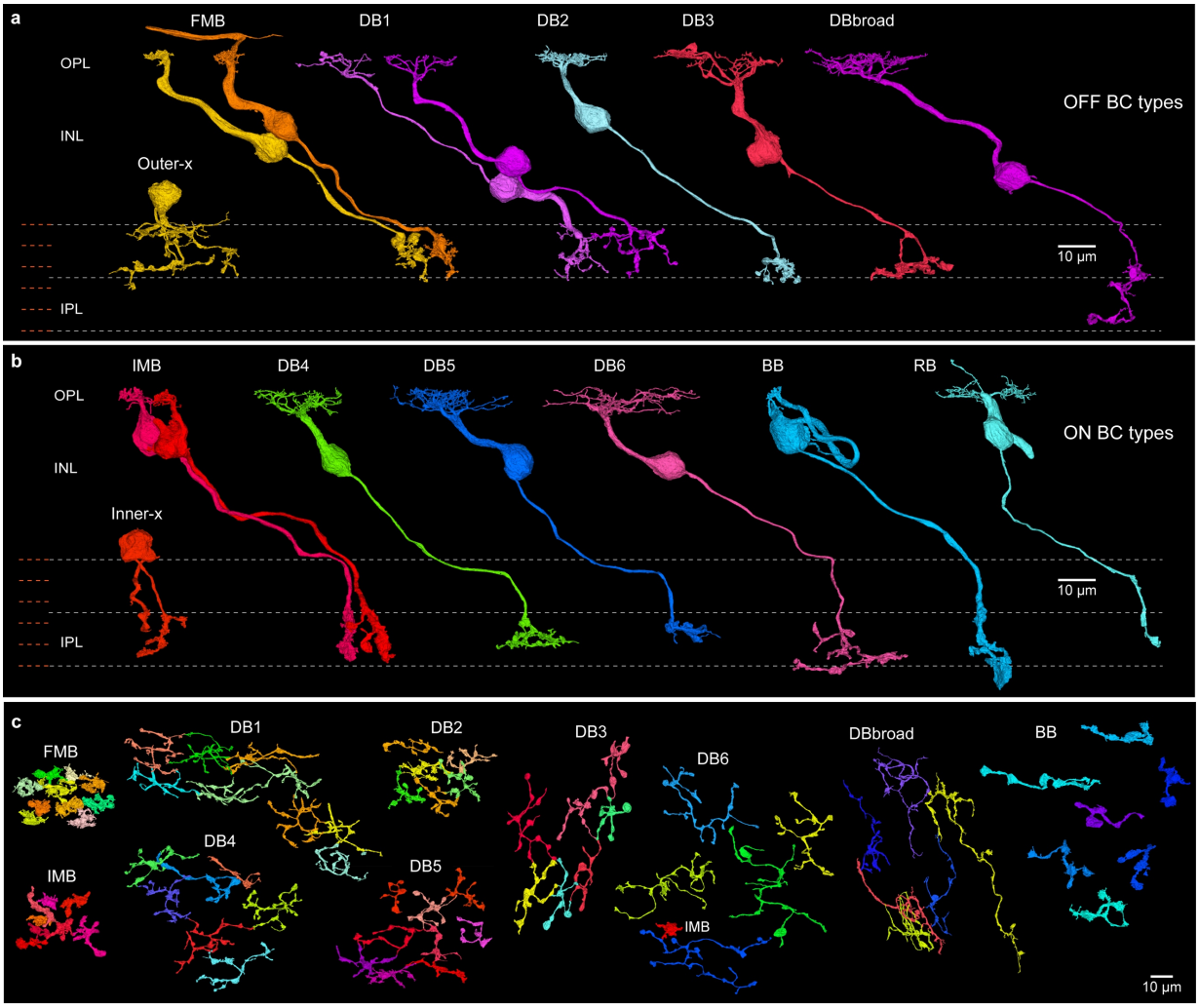

Fig. 4. Bipolar cell types. a. Outer stratifying types (FMB, flat midget bipolar; DB, diffuse bipolar). Outer-x bipolar cells lacked a dendrite but made ribbon synapses in the IPL (Supplementary Fig. 6a). DBbroad cells extend processes across the IPL depth (Supplementary Fig. 7). **b.** Inner stratifying bipolar types: IMB, invaginating midget bipolar; DB, diffuse bipolar types; BB, blue-cone bipolar type; Inner-x bipolar (Supplementary Fig. 6c); RB, rod bipolar. **c**. Horizontal view of spatial mosaics of axon terminals for small groups of neighboring cells of each bipolar type, as indicated.

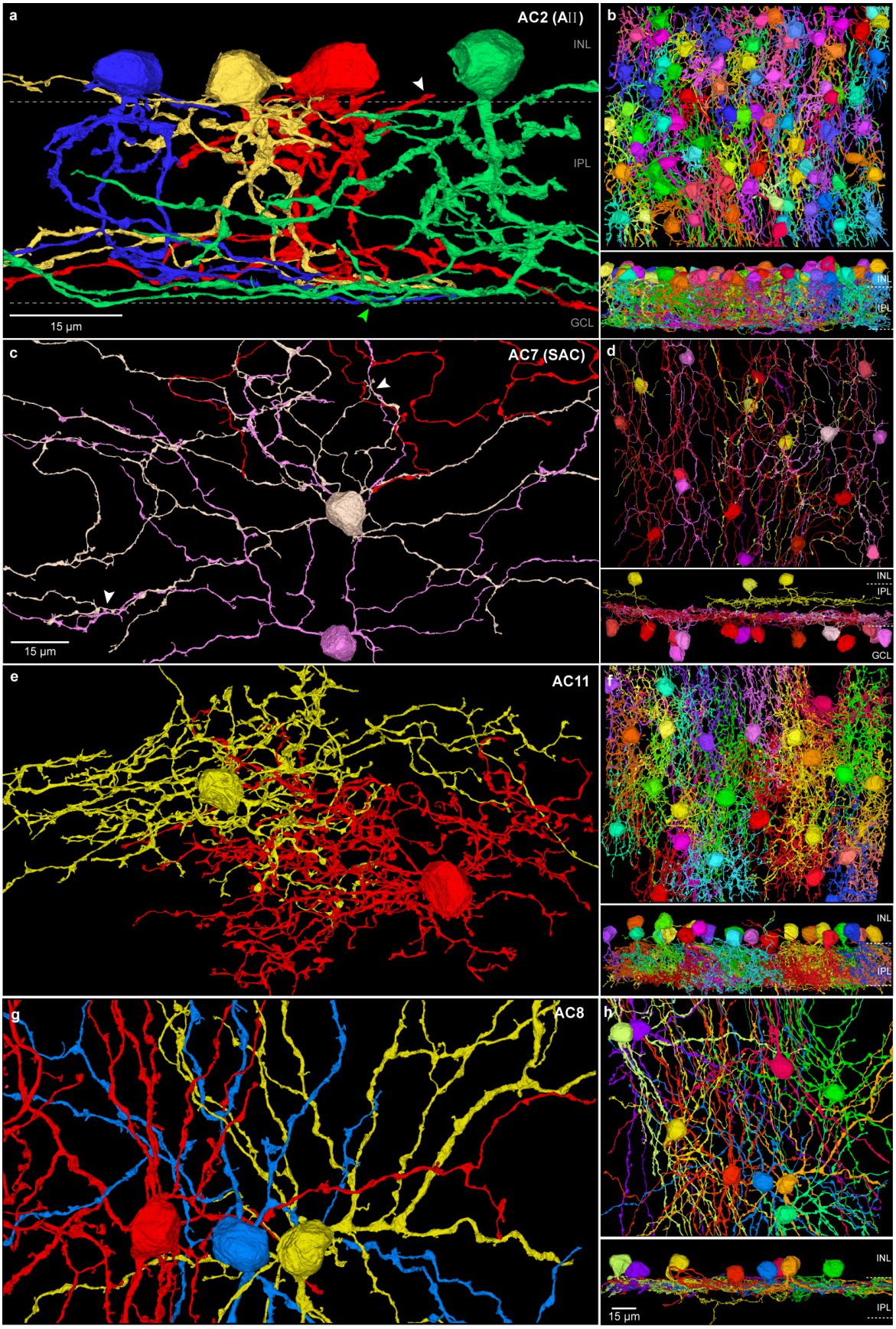
a
AC2 (AII)
INL
IPL
GCL
15 µm
b
INL
IPL
c
AC7 (SAC)
15 µm
d
INL
IPL
GCL
e
AC11
f
INL
IPL
g
AC8
h
INL
IPL
15 µm

503

504 **Fig. 5. Amacrine cells.** Amacrine cells in the INL (253 cells) and GCL (40 cells) were divided
505 into 19 types (AC1-19; Supplementary Table 1g). **a.** Small-field, AII amacrine cells (AC2), in
506 vertical view show outer, lobular dendrites (white arrowhead) and extensive, inner dendrites
507 (green arrowhead). **b.** Horizontal view of the entire AII population in HFseg1; lower panel,
508 vertical view. **c.** Starburst amacrine cells (AC7) were located primarily in the GCL (GCL, 14
509 cells; INL, 3 cells). White arrowheads indicate typical fasciculation of starburst dendrites. **d.**
510 Mosaic of starburst cells, with GCL cells (red-violet) and INL cells (yellow); lower panel,
511 vertical view. **e**. Small-field amacrine type (AC11) in horizontal view with densely branched
512 dendritic arbor. **f**. Horizontal view of the AC11 cell mosaic; lower panel, vertical view shows
513 dendrites extend broadly across the IPL. **g.** Large-field amacrine cells (AC8) with thick lobular
514 dendrites, narrowly stratified in the outer IPL. **h.** Horizontal view of the complete mosaic; lower
515 panel shows vertical view of outer IPL stratification. Scale bar in **c** applies to **e** and **g**. Scale
516 bar in lower panel of **h** applies to **b, d, f**.

517

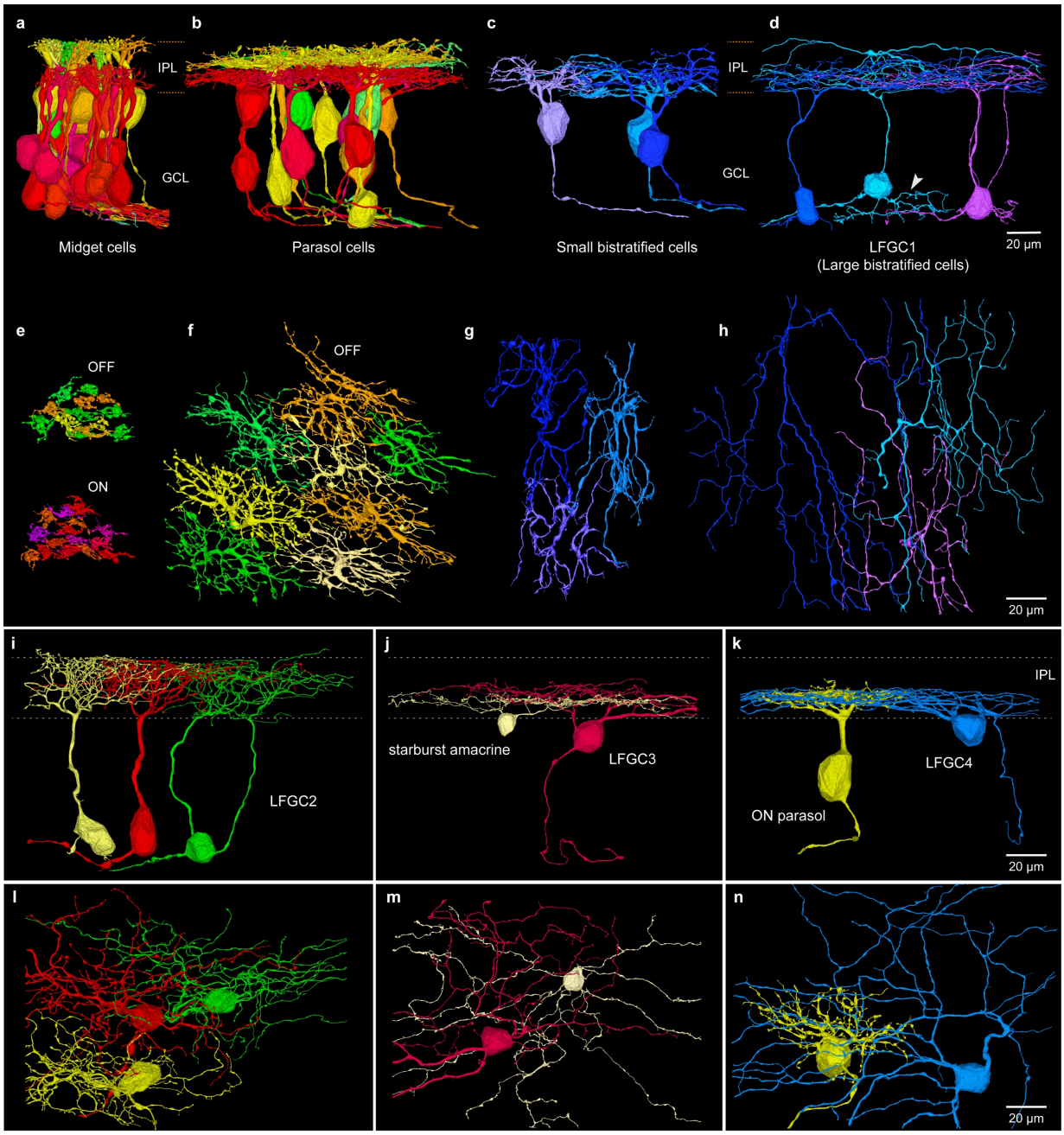

Fig. 6. Ganglion cells. a. Cluster of inner-ON (red-violet) and outer-OFF (yellow-green) midget ganglion cells; dendrites stratify broadly across inner (ON) and outer (OFF) half of the IPL. **b**. Inner-ON (red-violet) and outer-OFF (yellow-green) parasol ganglion cells; dendrites stratify broadly near the center of the IPL. **c**. Small bistratified ganglion cells extend dendrites across the ON-OFF subdivision of the IPL. **d**. Large bistratified ganglion cells (LBGC1) show large dendritic fields and broad stratification. White arrowhead shows branching processes

525 arising from the cell body of unknown significance. **e-h**, Mosaic of dendritic arbors in
526 horizontal view of the same cells shown in **a-d**. **e**. Outer-OFF (yellow-green, top) and inner-
527 ON (red-violet) midget GC. **f**. Outer-OFF parasol cell dendrites show minimal overlap (inner-
528 ON parasol mosaic not shown). **g**. Small bistratified cells show minimal dendritic tree overlap.
529 **h**. LFGC1 (Large bistratified cells) show a much larger and more sparsely branching irregular
530 tree. **i-k**. Morphology of three additional large field types. **i**. LFGC2 (Large diffuse cells) show
531 a densely branched tree broadly stratified across the IPL. **j**. LFGC3 (Recursive bistratified
532 cells) are narrowly bistratified near the center of the IPL and tend to fasciculate with starburst
533 amacrine cells. **k**. LFGC4 (Inner smooth monostratified cells) show large, monostratified
534 dendritic trees costratified with parasol cells. **l-n**. Horizontal views of the cells shown in **i-k.**

535

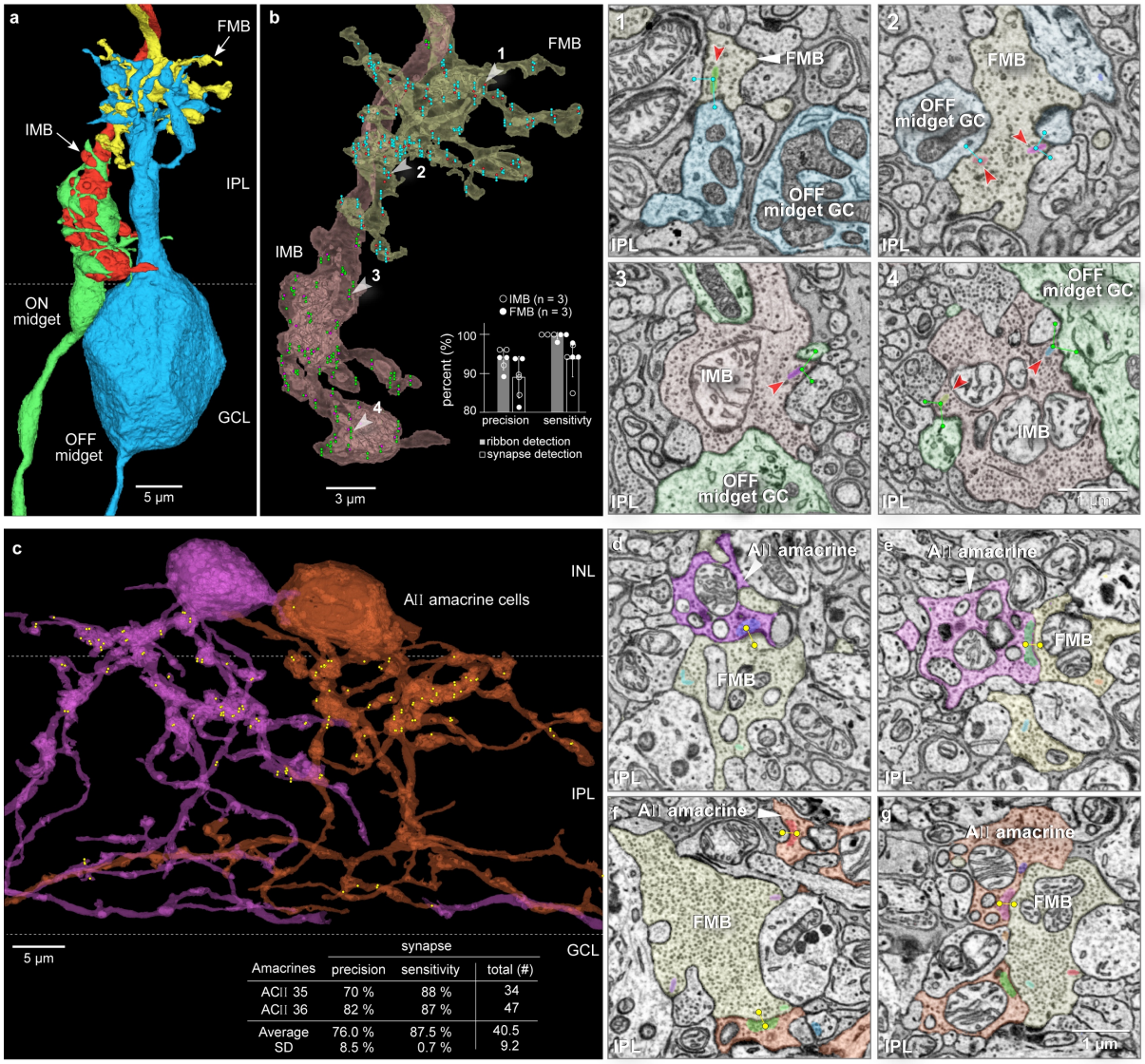

Amacrines	synapse precision	synapse sensitivity	total (#)
ACII 35	70 %	88 %	34
ACII 36	82 %	87 %	47
Average	76.0 %	87.5 %	40.5
SD	8.5 %	0.7 %	9.2

Fig. 7. Synapse detection. a. OFF midget bipolar (yellow) and ON midget bipolar (red) presynaptic to an outer-OFF (blue) and inner-ON (green) midget ganglion cell. **b.** Outgoing synapses detected for the midget bipolar cell axon terminals shown in **a** (ganglion cells removed, semi-transparent view). Synaptic ribbons (red/violet dots) and postsynaptic profiles were first identified manually (see Supplementary Fig. 9; cone 22; BC 308 (IMB) and BC 303 (FMB)). Predicted outgoing synapses (green dots and lines, IMB; blue dots and lines, FMB) are shown. White arrowheads numbered 1-4 indicate the panels shown on the right in single-layer EM view. Predicted and segmented synaptic ribbons (in varied colors, red arrowheads);

545 predicted postsynaptic segments are marked by the dots and lines linking the synaptic ribbon
546 to its postsynaptic structure (unlabeled postsynaptic profiles belong to amacrine cells). Inset
547 histogram shows precision and sensitivity of ribbon detection and synaptic assignment. **c.**
548 Inhibitory output synapses made by two neighboring AII amacrine cells (purple and orange,
549 shown in partial transparency). Yellow dots show synaptic output predictions; most synaptic
550 outputs arise in the outer half of the IPL and are presynaptic to OFF bipolar cells. Inset shows
551 precision and sensitivity for the synapses made by each AII cell. **d-e**. Single-layer images
552 showing segmented vesicle clouds (varied colors) in the purple AII cell (shown in **c**) and
553 synaptic connections predicted with an FMB cell (yellow dots and lines; ribbons in the FMB are
554 also segmented). **f-g**. Same conventions as in **d-e** but showing three segmented vesicle clouds
555 and synaptic predictions for the orange AII cell (shown in **c**), with another FMB cell.

556

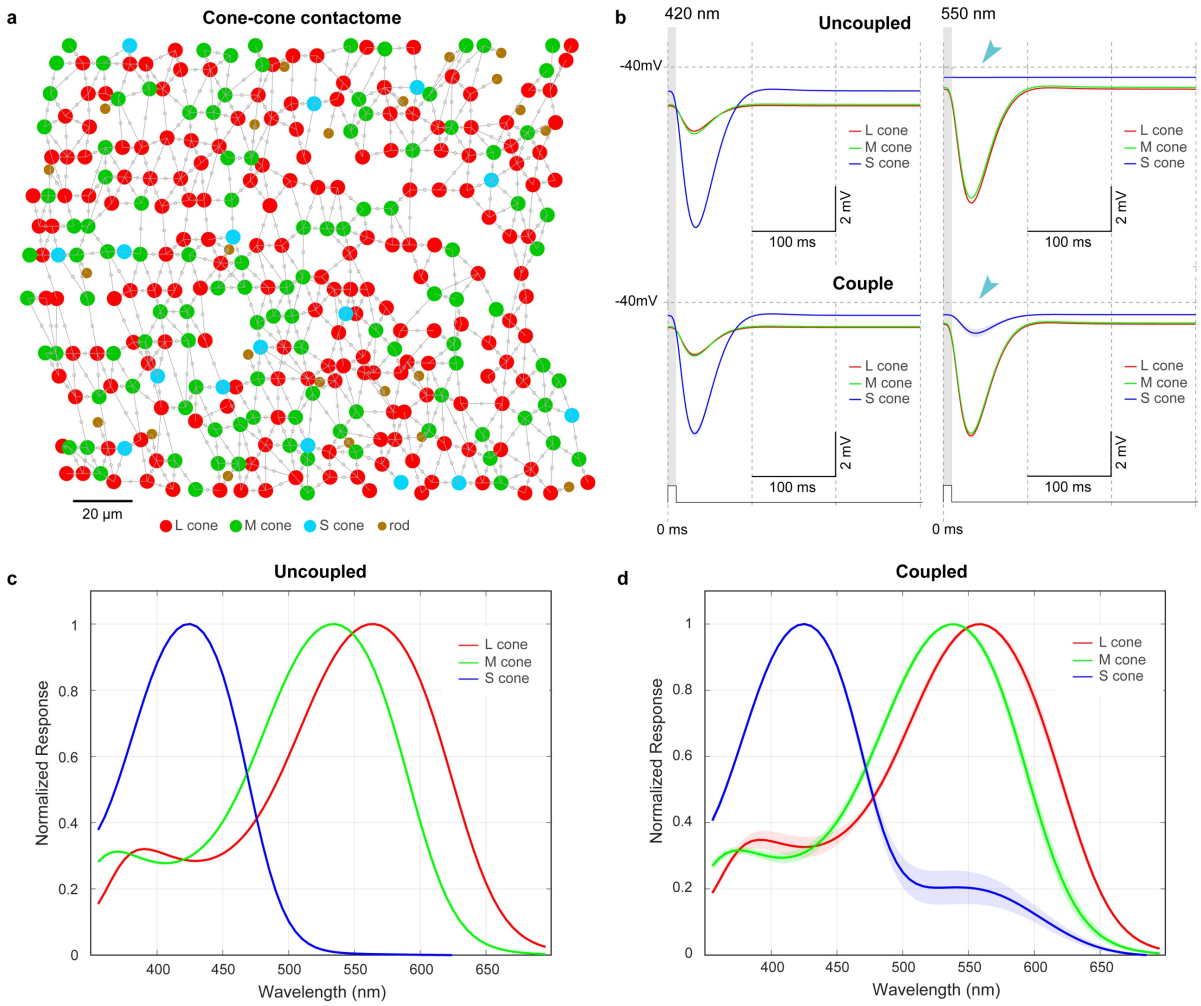

Fig. 8. Cone-cone coupling alters S cone spectral tuning. a. Biophysical model of the cone-cone connectome. Assignment of L/M cone type was random with a ~1.7:1 L:M ratio, based on known proportions in the human fovea. Contacts between cones were determined from the reconstructed connectome, and conductances were assigned based on the contact area, known density gap junction density, and single connexin channel conductance. Cones were modeled compartmentally as a soma that included the phototransduction cascade, connected to an axon, in turn connected to the axon terminal (see model parameters in Supplementary Table 4). **b**. Modeled voltage responses (averages from 5 different L, M and S cones in the network) to monochromatic 10 msec light flashes at 420 nm and 550 nm. **Top:** the cone-cone network is uncoupled (zero cone-cone conductance). **Bottom**: the network is coupled via the individual

568 cone-cone conductances given in the electrical model. Coupling among L, M, and S cones
569 produces a light-evoked response in S cones at 550 nm that is absent in the uncoupled
570 condition. **c**, **d**. Impact of cone-cone coupling on the action spectrum of the cone voltage
571 response. Average light responses were generated every 5 nm from 350 to 700 nm. In **c**
572 (uncoupled condition), the action spectrum is proportional to the spectral sensitivity of the L, M,
573 and S cone opsins. In **d** (coupled condition), the S cone voltage response shows a smaller
574 second peak of sensitivity at ~550 nm (teal arrowhead) which is not present when cones are
575 uncoupled.

576

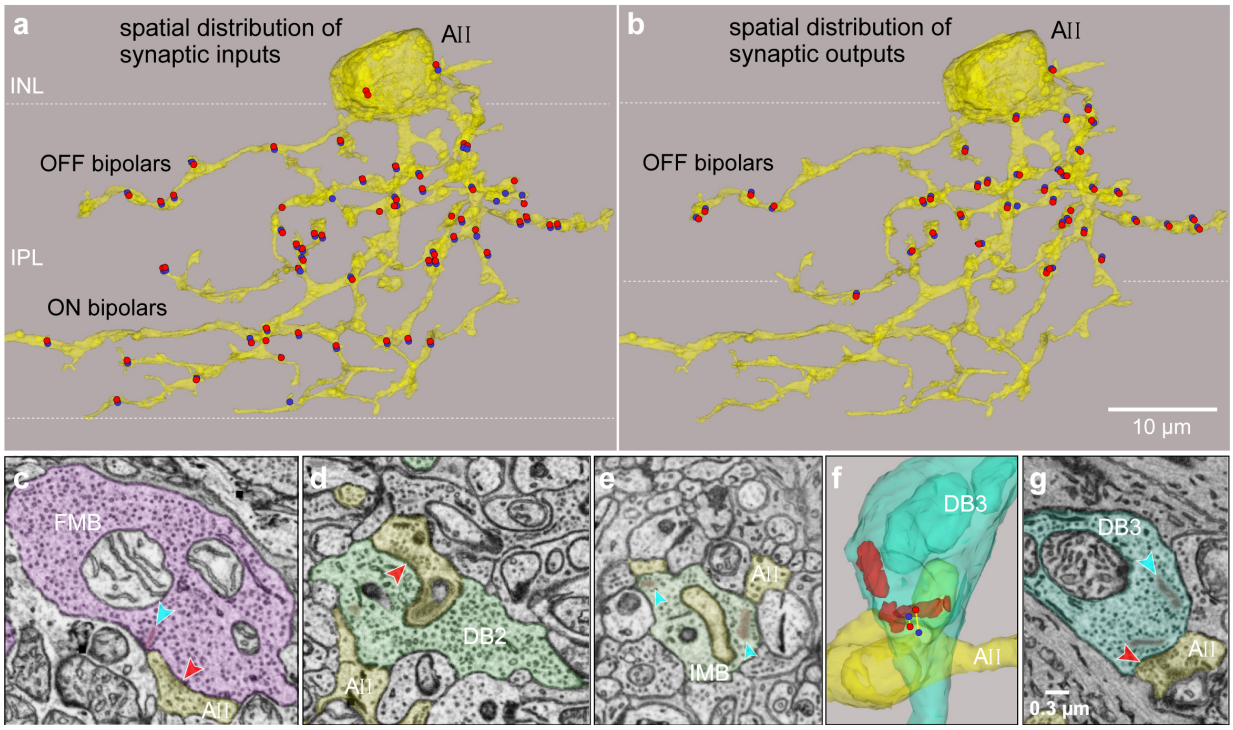

Fig. 9. AII cells are postsynaptic to both ON and OFF cone bipolar cells at ribbon synapses. a. Chemical (ribbon) synaptic inputs from multiple OFF and ON bipolar types. For this cell, 70 synapses (red dots, presynaptic locus; blue, postsynaptic locus; most blue postsynaptic dots are overlying the presynaptic position and are not visible in this zoomed-out view) are dispersed throughout the dendritic tree. We found 300 synapses arising from all ON and OFF cone bipolar types to an initial sample of 6 AII cells, with IMB and FMB cells accounting for 19% and 24% of the synapses respectively. **b**. By contrast, this AII cell is presynaptic only to OFF cone bipolar cells; many of these synapses are reciprocal. **c**. An OFF-midget bipolar (FMB, violet) makes a ribbon dyad synapse (blue arrowhead points to ribbon) with the AII cell (yellow) and a parasol ganglion cell. The AII cell makes a nearby reciprocal synapse (red arrowhead) upon this FMB. **d.** Nonreciprocal AII synapse with a DB2 OFF bipolar type (teal). **e.** AII cell (yellow) postsynaptic to an ON-midget bipolar (IMB, green) at two dyad synapses (blue arrowheads). **f**. 3D view of a reciprocal synapse between this AII and a DB3 bipolar (blue); the AII inserts a finger-like projection into this bipolar axon terminal.

592 **g**. Single section through contact in **f,** showing two of three ribbon synapses (blue arrowhead

593 indicates one) and the reciprocal AII inhibitory synapse (red arrowhead).

594

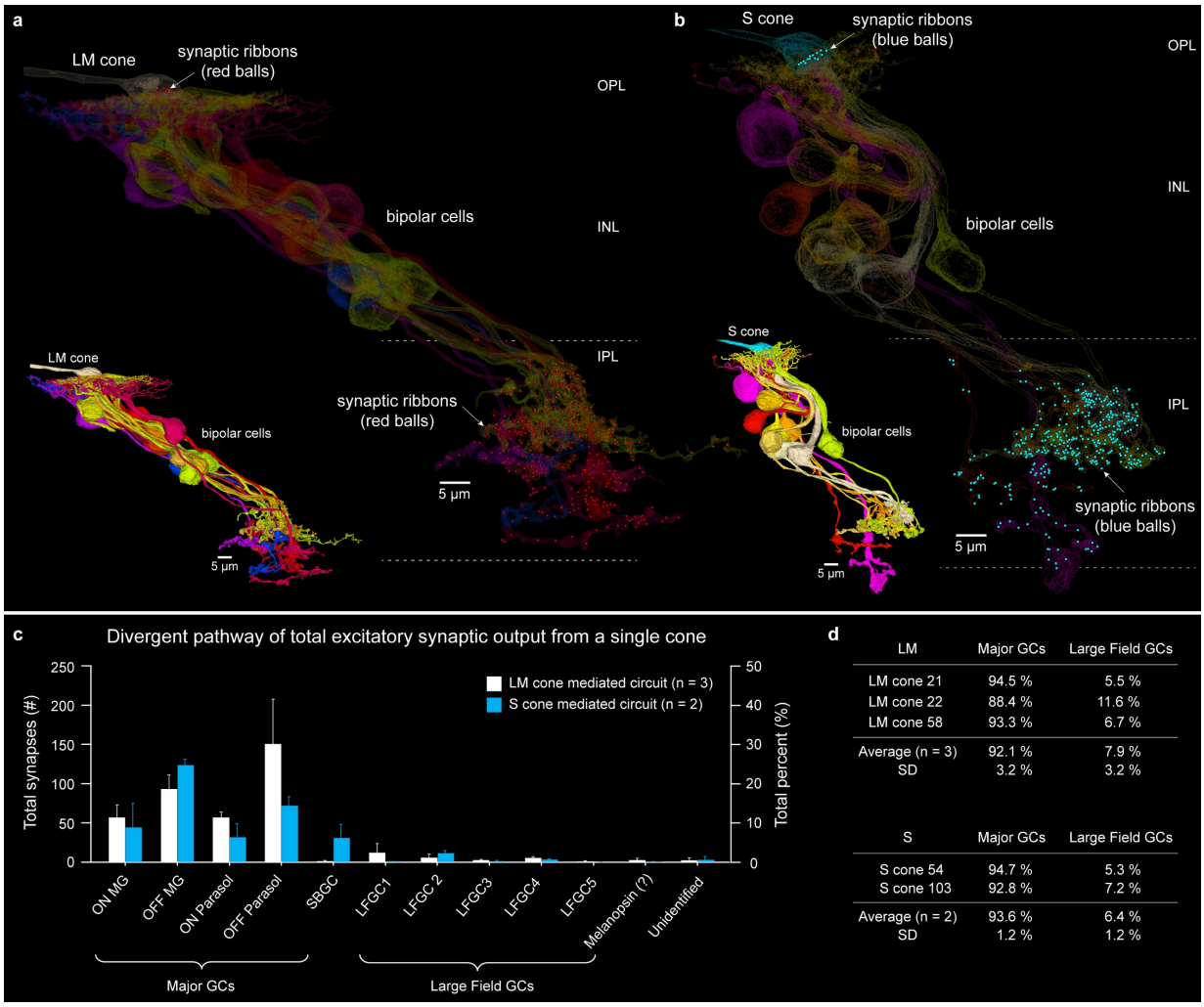

Fig. 10. Vertical excitatory connectome. a. Vertical connectome for a single LM cone (cone 22, see details in Supplementary Fig. 9b). Cone pedicle and postsynaptic bipolar cells shown in silhouette. Synaptic ribbons in the cone pedicle (top, OPL) and bipolar cell axon terminals (lower, IPL) are shown as red balls. Inset shows all bipolar cells postsynaptic to this cone pedicle (outer, yellow-gold; inner, blue-violet-red). **b**. The same views for an identified S-cone (cone 103, see details in Supplementary Fig. 10b; synaptic ribbons, blue dots). **c**. Histogram shows output synapse numbers (left axis), and percent (right axis) made via bipolar cells connected to 3 LM and 2 S cones to postsynaptic GC types. Note that OFF-pathway-derived synapses greatly outnumber ON pathway synapses. **d**. The great majority of synapses from LM and S cones are distributed to midget, parasol, and small bistratified ganglion cells (Major

606 GCs), with all other large-field types receiving 7.9% (LM) and 6.4% (S) of the synaptic output

607 (see also Supplementary Table 2). Unidentified processes account for 0.5% of the total

608 synaptic output (LM) (see Supplementary Table 2a-2c).

609

610 **Methods**

611 **EXPERIMENTAL MODEL AND SUBJECT DETAILS**

612 **Human tissue acquisition and preparation**

613 Human eyes (52-year-old, white male; brain dead organ donor) were acquired from the
614 Medical University of Vienna, Vienna, Austria at the time of death by surgical enucleation. A
615 small incision was made to give fixative access to the posterior chamber and the retina was in
616 this way immersion fixed in 4% glutaraldehyde in 0.1 M sodium cacodylate buffer, pH7.3-7.4 at
617 room temperature. Medical history confirmed no abnormalities of the visual system recorded
618 and no driving limitations; the ocular status was defined medically as unremarkable at time of
619 enucleation. Eyes were shipped in fixative to the University of Washington where the retinas
620 were dissected and prepared for electron microscopy.

621

622 **METHOD DETAILS**

623 **Identification of foveal ROI, serial block-face SEM sample preparation and image**
624 **acquisition**

625 Retinal tissue was dissected under a dissecting microscope to facilitate identification of the
626 optic disc and the center of the foveal pit as well as the major retinal meridians. We selected
627 an ROI that extends across absolute eccentricity of ~450-650 microns (temporal retina). This
628 location is linked to cones located ~100-300 microns from the foveal pit center due to the
629 lateral migration of retinal circuits from the cones at the foveal center. This location
630 encompasses much of the central 1 degree (~300 μm/deg) of visual angle (Fig. 1a-1c).

631 The dissected retina was then plastic embedded and prepared for electron microscopy as
632 previously described[1]. In brief, the tissue was incubated in a 1.5% potassium ferrocyanide and
633 2% osmium tetroxide (OsO4) solution for 1 h. After washing, the tissue was placed in a freshly

634 made thiocarbohydrazide solution for 20 min and then rinsed and incubated in 2% OsO4 for
635 30 min. Lastly, the tissue was stained en bloc in 1% uranyl acetate overnight and
636 subsequently stained with Walton's lead aspartate, dehydrated and plastic embedded
637 (Durcupan, 44610, Sigma Aldrich). After evaluation of the ROI by semithin sectioning the
638 tissue block was trimmed, gold-coated by standard methods, and mounted in an Apreo SEM
639 Volumescope (Thermo Fisher). We cut 3028 sections at 50 nm thick for a total depth of ~150
640 microns, imaging an ROI (180 μm tall x 180 μm wide; 5 nm pixels) that encompassed the full
641 vertical depth of the retina, from the Henle fiber layer (HFL) to the nerve fiber layer (Fig. 1d).
642 The overall ROI was imaged on the blockface after each section as 25 sequential tiles (8000 x
643 8000 pixels or 40 x 40 μm; 75,700 total image tiles) with 10% overlap. Images were stitched
644 within layer and aligned across layers using standard methods available in TrakEM2[2] (NIH
645 image plugin; Scale Invariant Feature Transform (SIFT) with affine translation) to create a
646 good quality volume. We first evaluated this TrakEM2-aligned volume by manual
647 reconstruction of a small number of selected cells and circuits[106]. To further develop this
648 volume as a connectomic resource we applied deep-learning based computational
649 approaches to realign, segment and reconstruct all cells and synaptic connections as
650 follows[20, 39].

651 **Volume creation**

652 *Montaging.* Tile offsets were determined manually, then refined by template matching at 40 nm
653 with a search window of 96 pixels. Tiles were cropped by 128 pixels to avoid edge distortions
654 and placed to minimize the sum of least squares from the new offsets. Outliers were inspected
655 and given manual placement. These cropped tiles were processed to create a pyramid of
656 encodings for resolutions between 20 nm and 640 nm[107], and then stitched to make the
657 montaged section in two steps. In the first step, only the two neighboring tiles in Y were
658 considered, with both neighbors being fixed. Using an online finetuner pyramid[107] with the

659 calculated placement as the starting point, a displacement field was generated that would
660 warp the encoded tiles to minimize the pixel difference with the fixed tiles. The encoded tiles
661 were then warped using this displacement field, eroded by a pixel to avoid partial pixels at the
662 edge, blended to the fixed tiles using the mean of the pixel values in the overlap, and then
663 passed through CLAHE (Contrast Limited Adaptive Histogram Equalization) enhancement to
664 mitigate the contrast loss from the warping and blending, resulting in strips of encoded tiles
665 where every other tile had been warped. In the second step, the strips of tiles from the first
666 step were stitched to each other, holding every other strip fixed in a similar process. An error
667 map was generated at both steps by computing the difference between the encodings in the
668 overlap at 40 nm and inspected. The non-encoded tiles were cropped by 394 pixels, warped
669 according to the composed displacement fields from the encodings, and combined to yield
670 montaged sections.

671 *Alignment.* The unaligned sections were first processed to create a pyramid of encodings[107]. A
672 rigid transformation for the entire dataset was estimated using SIFT features[108] extracted from
673 the encodings at 640 nm and correspondences established between nearest and next-nearest
674 section pairs. From the rigidly aligned encodings, displacement fields at 40 nm resolution were
675 generated between nearest and next-nearest section pairs using an online finetuner
676 pyramid[107].

677 A convolutional net trained to detect local misalignments and/or simple mismatches caused by
678 defects in the EM images was used to mask unreliable regions in each displacement field. In
679 addition, 25 sections with defects that presented with non-smooth deformations were masked
680 by hand. Pairwise displacement fields and transformation masks were then passed to a global
681 relaxation[107, 109]. This relaxation was performed first at 2560 nm across all 3028 sections of the
682 dataset, and subsequently in blocks of approximately 100 sections at a resolution of 640 nm,
683 using the previously generated drift-free fields as constraints for the start and end sections of

684 each of the 31 blocks. The resulting displacement fields were composed with the earlier rigid
685 transformation and the final aligned image stack warped and rendered at 10 nm.

686 *Segmentation.* We pretrained a convolutional net to predict affinities between neighboring
687 voxels at 16×16×40 nm³ using 1,368 µm³ of manually annotated data derived from three
688 mouse visual cortex datasets[110]. We used the residual symmetric U-Net architecture[111] with
689 modifications[112] and trained with data augmentation previously described [113]. The network was
690 trained for 2,000,000 iterations using four NVIDIA L4 GPUs with PyTorch data parallelism,
691 where each GPU processed individual patches with its own model replica.

692 To further fine-tune this network, we manually created training data consisting of 39 µm³ at a
693 resolution of 20×20×50 nm³. In contrast to the pretraining datasets, mitochondria were
694 intentionally over segmented to bias boundary detection toward a more conservative
695 approach, aiming primarily to reduce merge errors at the expense of increasing split errors.
696 We fine-tuned the network for 300,000 iterations.

697 We predicted an affinity map for the whole dataset. Dark voxels could sometimes span
698 multiple cells and cause segmentation errors. We therefore applied a binarized mask for dark
699 voxels with a threshold of 0.2, invalidating each dark voxel and its three incident affinities. The
700 resulting masked affinity map was then segmented with a mean affinity agglomeration
701 threshold of 0.25[113]. The segmentation was ingested into the Connectome Annotation
702 Versioning Engine proofreading platform, CAVE[114] for further analysis.

703 CAVE permitted proofreading to be performed by a user community accessing the web-based
704 neuroglancer interface[113, 115] with dynamic updating of segment ID and related synaptic
705 connectivity. The HFseg 1 segmentation was of high initial quality such that it was possible to
706 identify and annotate all major cell classes within the volume and to sort these cells into

707 populations of distinct types using the annotation tools available in neuroglancer. All cells are
708 accessible at NeuroMaps (https://neuromaps.app).

709 Cell types were identified provisionally based on segment 3D morphology (dendritic
710 morphology, stratification depth, and spatial regularity and interaction (mosaics) and in some
711 cases nuclear morphology). Four of the authors (Kim, Dacey, Grünert and Martin) conferred
712 and agreed on cell type identification. Proofreading is ongoing (~ 40,000 edits) and applied
713 thus far primarily to correct larger obvious mergers (primarily with glial cell processes) that
714 interfered with cell type identification and additional more detailed proofreading on circuits of
715 interest in the current survey of cone-bipolar-ganglion cell connections. Many cell populations
716 were unambiguously recognized based on previous studies of primate retina[41, 116, 117] (e.g., the
717 S cones, rods and LM cones, the H1 and H2 horizontal cells, the starburst and AII amacrine
718 cell types, the midget, diffuse, blue-cone bipolar, and rod bipolar types, or the midget, parasol
719 and small bistratified and large bistratified ganglion cell types; Müller glia, astrocytes and
720 microglia); some cell types (the low-density amacrine types) were provisionally designated
721 subject to further proofreading and connectivity analysis. Following FlyWire[40], we have
722 initiated an open community of retinal neurobiologists (currently 7 labs participating) to use
723 these tools to complete proofreading of the HFseg1 volume.

724 **Synapse detection**

725 *Ribbon synapse detection in OPL and IPL*. A symmetric residual U-Net architecture was
726 trained on data with a resolution of 10×10×50 nm^3 using input patches of size
727 128×128×20 to generate a probability map that indicates the likelihood of each voxel
728 belonging to a synaptic ribbon [118]. To remove less robust predictions at the boundaries,
729 only the central 96×96×16 voxels of the input patch was used as the output. The model

730 was trained on a total volume of 2,254 μm^3 of manually labeled cutouts sampled from
731 various regions across the entire dataset.

732 The ribbon segmentation was produced by (1) down sampling the probability map by 2×, (2)
733 thresholding for voxels above 0.15, and (3) using 26-connectivity to extract connected
734 components. Segments smaller than 5 voxels in a 20×20×50 nm^3 resolution were neglected to
735 eliminate spurious detections.

736 To achieve ribbon detection in the OPL segments smaller than 5 voxels (in a 20×20×50 nm^3
737 resolution volume) were first disregarded to eliminate spurious detections of extremely small
738 ribbon-like structures. For each detected ribbon within a cone pedicle, postsynaptic partners
739 were identified via the following steps: (1) All neighboring segments touching the pedicle
740 within 800 nm of the ribbon centroid were identified. (2) For each neighbor, a representative
741 point close to the ribbon was chosen as the postsynaptic site. These constitute the set of
742 putative synapses for each ribbon. (3) After cell identification, only putative synapses onto
743 bipolar or horizontal cells were kept; all others were filtered out (e.g. Müller glia, neighboring
744 cones, mitochondria). (4) Finally, for each distinct ribbon-postsynaptic cell pair, all but the
745 shortest putative synapse were filtered out. The result was that a single synaptic connection
746 was found onto any bipolar or horizontal cell contacting that cone pedicle within 800 nm of a
747 given cone ribbon.

748 For synaptic ribbons in the IPL, segments smaller than 5 voxels in a 20×20×50 nm^3 resolution
749 within the bounds of the IPL were also disregarded to eliminate spurious detections. For each
750 detected ribbon, postsynaptic partners were automatically identified via the following steps: (1)
751 Identify the two largest cells within a small (500 nm) window of the centroid of the ribbon
752 which are adjacent to the presynaptic cell and are also adjacent to each other. (2) If such a
753 pair is found, the ribbon is assumed to be presynaptic to both (i.e., a dyadic synapse). (3) If no

754 such pair is found, then within the window, the single largest profile adjacent to the
755 presynaptic cell is identified as the postsynaptic partner. (4) Putative synaptic connections
756 were filtered by cell type, requiring the presynaptic cell to be previously annotated as a bipolar
757 cell, and the postsynaptic partner to be previously annotated as amacrine, or ganglion cell.
758 Note we did not at this time try to use a convolutional net to detect a low density of possibly
759 ribbonless synapses.

760 *Vesicle cloud detection and conventional synapse assignment in the IPL.* A symmetric residual
761 U-Net architecture was trained on data with a resolution of 10×10×50 nm^3 using input patches
762 of size 128×128×20 to generate a probability map that indicates the likelihood of each voxel
763 belonging to a vesicle cloud[118]. To remove less robust predictions at the boundaries, only the
764 central 96×96×16 voxels of the input patch was used as the output. The model was trained on
765 a total volume of 2,254 μm^3 of manually labeled cutouts sampled from various regions across
766 the entire dataset (the same cutouts as ribbon synapse detection). Manual labels were
767 roughly annotated to mark approximate locations of vesicle clouds rather than precise
768 boundaries.

769 The vesicle cloud segmentation was produced by (1) downsampling the probability map by
770 2×, (2) thresholding for voxels above 0.15, and (3) using 26-connectivity to extract connected
771 components. Segments with fewer than 200 voxels were excluded, based on the range of
772 vesicle cloud sizes encountered.

773 *IPL conventional synapse assignment*. A symmetric residual U-Net architecture was trained on
774 data with a resolution of 20×20×50 nm^3 using input patches of size 24×24×8 to generate a
775 probability map that indicates the likelihood of each voxel belonging to the postsynaptic cell[118].
776 The model was trained on 682 μm^3 of manually annotated labeled cutouts.

777 The model was applied once for each vesicle cloud detected, in a window centered on the
778 centroid of the vesicle cloud. Using the initial automatic cell segmentation, the cell with the

779 highest mean probability within the window was selected as the putative postsynaptic
780 partner[118]. Further filtering by cell type was applied, requiring the presynaptic cell to be
781 previously annotated as an amacrine cell, and the postsynaptic partner to be previously
782 annotated as amacrine, bipolar, or ganglion cell.

783 **Building and modeling the cone-cone contactome**

784 *Generating the cone-cone contactome.* We identified gap junctions between cone pedicles
785 and between cone pedicles and rods as follows. Cones and rods were manually identified and
786 proofread to completion. Contacts were computed using a recently developed supervoxel
787 agglomeration process (abiss)[119] where a contact is considered to be a set of connected voxel
788 faces that are shared by the same pair of segments. For each contact, we counted the
789 number of voxel faces along each orientation (xy, xz, and yz), as well as the minimum
790 bounding box containing all of the faces. The surface area of a contact was estimated by
791 computing the sum of the area of all faces involved. Contacts were excluded from analysis if
792 (1) the surface area of the contact was $\leq$0.04 μm^2 (mean surface area of contact, 0.55 ± 0.3
793 μm^2, n = 1141 cone-cone contacts) or (2) the center of the bounding box was more than 15
794 μm from the approximate center of the cone pedicle (manually identified). All remaining
795 contacts were manually inspected with 1× coverage to determine if they corresponded to what
796 would be manually identified as a true cone-cone contacts harboring gap junctions.

797 *Biophysical modeling of cone-cone contactome***.** To generate a biophysical model of the
798 electrically coupled photoreceptor network, we started with data from the X,Y locations of 310
799 cone and 24 rod synaptic terminals, and for the cones their M/L vs. S identity. We then
800 incorporated all reviewed and accepted cone-cone contacts and the surface areas of each
801 contact.
802

803 The cone morphology was modeled as a sphere (single compartment, dia. 2.5 μm) for the
804 outer and inner segments and soma, connected to an axon (dia. 1.6 μm, Ri 80 Ohm-cm, Rm
805 12,000 Ohm-cm^2 [7] ; V_{rev} -60 mV, compartment size 0.05 lambda, ~9 compartments/cone
806 axon) extending 300 μm to the terminal (diam 5 μm, Rm 12,000 Ohm-cm^2, V_{rev} -60mV). Rod
807 morphology was similar (OS/IS diam 2.5 μm, axon dia 0.45 μm, terminal dia. 3 μm). The
808 OS/IS/soma compartment contained a transduction mechanism (max conductance 880 pS)
809 with spectral sensitivity appropriate for the cone identity. The transduction mechanism of the
810 photoreceptor biochemical cascade generated a peak ~20 ms after the stimulus with a
811 damped recovery [8-15]. Spectral sensitivity for the L/M cones was taken from non-human
812 primate[9] and for the S cones from human cone data (peak sens. 420 nm[16] corrected for lens
813 spectral sensitivity[17]). In some models including both lens and macular filters, the S cone peak
814 sensitivity was shifted to ~440 nm.
815
816 The location of all the S-cones and rods in the reconstructed contactome was known but the
817 individual identity of L/M cones was unknown, so for the simulations the L/M identity was set
818 randomly. The target L/M ratio was 1.7 and the actual L/M ratio in the model shown was
819 1.697. The contacts between cones had not been resolved into gap junctions (groups of
820 connnexin molecules), but the area of each contact had been measured. The conductance for
821 each contact was calculated by taking the average area of the contacts (0.55 μm^2), assuming
822 5 connexins[18] (15 pS per connexin) per average contact[19,20] to produce an average
823 conductance of 75 pS, or 136 pS/μm^2. The conductance for each individual contact was then
824 calculated by multiplying by the contact area. Contacts were simulated with a linear gap
825 junction conductance (i.e. electrical synapse). The cones had on average 3.6 contacts with
826 neighboring cones. The average L/M total coupling conductance was ~270 pS, and for S-LM
827 cones was ~282 pS. There were a total of 715 coupled pairs of cones, 659 LM pairs, and 56
828 pairs with 1 S cone. The average coupling conductance between adjacent pairs of L/M cones

was 116 pS, and for L/M–S pairs was 123 pS. However, the average measured coupling conductance between LM pairs was 133 pS (n = 25) and between S-LM pairs was 166 pS (n = 14) due to the existence of multiple current paths between pairs through the gap junction network. The average cone terminal input resistance was ~0.4 Gohm.

The simulated cones were stimulated with flashes of monochromatic light (10 ms, 1000 μm spot, ~1e5 Ph/μm^2/sec) on a white background (1e4 Ph/μm^2/s, spectrally flat). The resting potential V_{rest} in response to the background was ~ -40 mV but varied by ~0.3mV depending on the cone identity and coupling. The flash response varied from 0 to -5 mV. To determine the effect of the gap junctions, simulations were run with the gap junction conductance at 0%, 50%, 100%, and multiples of the nominal 136pS/μm^2 conductance. The model was constructed in the Neuron-C simulation language [21] and comprised ~3000 compartments. The model was run on AMD Opteron 3000 MHz CPUs under the Linux and Mosix operating systems. Approximately 200 simulations were run of the 310-cone model to develop and calibrate the model. Modeling code can be accessed at zenodo.org upload of Neuron-C at: https://doi.org/10.5281/zenodo.17792059.

Proofreading, synaptic connectivity and updating with the Connectome Annotation Versioning Engine (CAVE) and NeuroMaps.

As noted above we ingested synapse predictions and cell type annotations into CAVE. A critical functionality given by CAVE is that is allows collaborative users to programmatically query the up-to-date proofread connectivity graph (synaptic connectivity is updated during proofreading of each segment-cell type) as well as any changes made to the metadata (cell type IDs, descriptions, or other annotations). We then adapted NeuroMaps to combine this

metadata with synaptic connectivity for each segment ID and to permit synaptic proofreading (addition or deletion of specific synaptic predictions).

DATA AND SOFTWARE AVAILABILITY

The HFseg1 dataset (volume, segmentation, synaptic detection and full annotation) are currently hosted by Zetta.ai (https://zetta.ai/) and all data is accessible for community proofreading by permission at NeuroMaps. The latest version of the HFseg1 dataset is also available for interrogation at NeuroMaps (https://neuromaps.app). Modeling code can be accessed at zenodo.org upload of Neuron-C at: https://doi.org/10.5281/zenodo.17792059

References

1. Ramon y Cajal S. La rètine des vertèbrès. *La Cellule* **9**, 119-257 (1892).

2. Masland RH, Raviola E. Confronting complexity: strategies for understanding the microcircuitry of the retina. *Annual review of neuroscience* **23**, 249-284 (2000).

3. Dowling JE. *The Retina: An approachable part of the brain*, 2nd edn. Harvard University Press (2012).

4. Rodieck RW. *The First Steps in Seeing*. Sinauer Associates, Inc. (1998).

5. Helmstaedter M, Briggman KL, Turaga SC, Jain V, Seung HS, Denk W. Connectomic reconstruction of the inner plexiform layer in the mouse retina. *Nature* **500**, 168-174 (2013).

6. Kim JS*, et al.* Space-time wiring specificity supports direction selectivity in the retina. *Nature* **509**, 331-336 (2014).

7. Briggman KL, Helmstaedter M, Denk W. Wiring specificity in the direction-selectivity circuit of the retina. *Nature* **471**, 183-188 (2011).

8. Anderson JR*, et al.* Exploring the retinal connectome. *Molecular vision* **17**, 355-379 (2011).

9. Calkins DJ, Schein SJ, Tsukamoto Y, Sterling P. M and L cones in macaque fovea connect to midget ganglion cells by different numbers of excitatory synapses. *Nature* **371**, 70-72 (1994).

10. Calkins DJ, Sterling P. Absence of spectrally specific lateral inputs to midget ganglion cells in primate retina. *Nature* **381**, 613-615 (1996).

11. Shekhar K*, et al.* Comprehensive Classification of Retinal Bipolar Neurons by Single-Cell Transcriptomics. *Cell* **166**, 1308-1323 e1330 (2016).

12. Peng YR*, et al.* Molecular Classification and Comparative Taxonomics of Foveal and Peripheral Cells in Primate Retina. *Cell* **176**, 1222-1237 (2019).

13. Yan W*, et al.* Cell Atlas of The Human Fovea and Peripheral Retina. *Sci Rep* **10**, 9802 (2020).

14. Hahn J*, et al.* Evolution of neuronal cell classes and types in the vertebrate retina. *Nature* **624**, 415-424 (2023).

15. Li J*, et al.* Integrated multi-omics single cell atlas of the human retina. *Res Sq*, (2023).

16. Dorkenwald S*, et al.* Neuronal wiring diagram of an adult brain. *Nature* **634**, 124-138 (2024).

17. Azevedo A*, et al.* Connectomic reconstruction of a female Drosophila ventral nerve cord. *Nature* **631**, 360-368 (2024).

18. Shapson-Coe A*, et al.* A petavoxel fragment of human cerebral cortex reconstructed at nanoscale resolution. *Science* **384**, eadk4858 (2024).

19. Loomba S*, et al.* Connectomic comparison of mouse and human cortex. *Science* **377**, eabo0924 (2022).

20. Turner NL*, et al.* Reconstruction of neocortex: Organelles, compartments, cells, circuits, and activity. *Cell* **185**, 1082-1100 e1024 (2022).

21. Ding Z*, et al.* Functional connectomics reveals general wiring rule in mouse visual cortex. *Nature* **640**, 459-469 (2025).

22. Abbott LF*, et al.* The Mind of a Mouse. *Cell* **182**, 1372-1376 (2020).

23. Lichtman JW, Sanes JR. Ome sweet ome: what can the genome tell us about the connectome? *Current opinion in neurobiology* **18**, 346-353 (2008).

24. Wandell BA, Dumoulin SO, Brewer AA. Visual field maps in human cortex. *Neuron* **56**, 366-383 (2007).

25. Sereno MI, Sood MR, Huang RS. Topological Maps and Brain Computations From Low to High. *Frontiers in systems neuroscience* **16**, 787737 (2022).

26. Harvey BM, Dumoulin SO. The relationship between cortical magnification factor and population receptive field size in human visual cortex: constancies in cortical architecture. *J Neurosci* **31**, 13604-13612 (2011).

27. Sereno MI*, et al.* Borders of multiple visual areas in humans revealed by functional magnetic resonance imaging. *Science* **268**, 889-893 (1995).

28. Schira MM, Tyler CW, Breakspear M, Spehar B. The foveal confluence in human visual cortex. *J Neurosci* **29**, 9050-9058 (2009).

29. Baden T, Berens P, Franke K, Roman Roson M, Bethge M, Euler T. The functional diversity of retinal ganglion cells in the mouse. *Nature* **529**, 345-350 (2016).

30. Bae JA*, et al.* Digital Museum of Retinal Ganglion Cells with Dense Anatomy and Physiology. *Cell* **173**, 1293-1306 e1219 (2018).

31. Goetz J*, et al.* Unified classification of mouse retinal ganglion cells using function, morphology, and gene expression. *Cell reports* **40**, 111040 (2022).

32. Masri RA, Percival KA, Koizumi A, Martin PR, Grünert U. Survey of retinal ganglion cell morphology in marmoset. *J Comp Neurol* **527**, 236-258 (2019).

33. Kim YJ*, et al.* Origins of direction selectivity in the primate retina. *Nature communications* **13**, 2862 (2022).

34. Curcio CA, Sloan KR, Kalina RE, Hendrickson AE. Human photoreceptor topography. *JCompNeurol* **292**, 497-523 (1990).

35. Curcio CA, Kar D, Owsley C, Sloan KR, Ach T. Age-Related Macular Degeneration, a Mathematically Tractable Disease. *Investigative ophthalmology & visual science* **65**, 4 (2024).

36. Schein SJ. Anatomy of macaque fovea and spatial densities of neurons in foveal representation. *J Comp Neurol* **269**, 479-505 (1988).

37. Drasdo N, Millican CL, Katholi CR, Curcio CA. The length of Henle fibers in the human retina and a model of ganglion receptive field density in the visual field. *Vision Res* **47**, 2901-2911 (2007).

38. Masri RA, Grünert U, Martin PR. Analysis of Parvocellular and Magnocellular Visual Pathways in Human Retina. *J Neurosci* **40**, 8132-8148 (2020).

39. Lee K, Turner N, Macrina T, Wu J, Lu R, Seung HS. Convolutional nets for reconstructing neural circuits from brain images acquired by serial section electron microscopy. *Current opinion in neurobiology* **55**, 188-198 (2019).

40. Dorkenwald S*, et al.* FlyWire: online community for whole-brain connectomics. *Nature methods* **19**, 119-128 (2022).

41. Grünert U, Martin PR. Cell types and cell circuits in human and non-human primate retina. *Progress in retinal and eye research*, 100844 (2020).

42. Grünert U, Martin PR. Morphology, Molecular Characterization, and Connections of Ganglion Cells in Primate Retina. *Annu Rev Vis Sci* **7**, 73-103 (2021).

43. Zhang L*, et al.* Evolutionary and developmental specialization of foveal cell types in the marmoset. *Proceedings of the National Academy of Sciences of the United States of America* **121**, e2313820121 (2024).

44. Kim YJ, Packer O, Pollreisz A, Martin PR, Grünert U, Dacey DM. Comparative connectomics reveals noncanonical wiring for color vision in human foveal retina. *Proceedings of the National Academy of Sciences of the United States of America* **120**, e2300545120 (2023).

45. Dacey DM. The mosaic of midget ganglion cells in the human retina. *JNeurosci* **13**, 5334-5355 (1993).

46. Dacey DM. Morphology of a small-field bistratified ganglion cell type in the macaque and human retina. *Visual neuroscience* **10**, 1081-1098 (1993).

47. Dacey DM, Lee BB. The blue-ON opponent pathway in primate retina originates from a distinct bistratified ganglion cell type. *Nature* **367**, 731-735 (1994).

48. Chichilnisky EJ, Baylor DA. Receptive-field microstructure of blue-yellow ganglion cells in primate retina. *NatNeurosci* **2**, 889-893 (1999).

1015 49. Calkins DJ, Tsukamoto Y, Sterling P. Microcircuitry and mosaic of a blue-yellow
1016 ganglion cell in the primate retina. *JNeurosci* **18**, 3373-3385 (1998).

1017

1018 50. Masri RA, Greferath U, Fletcher EL, Martin PR, Grünert U. Immunohistochemistry and
1019 spatial density of Müller cells in the human fovea. *Investigative ophthalmology & visual*
1020 *science* **in press**, (2025).

1021

1022 51. Singaravelu J, Zhao L, Fariss RN, Nork TM, Wong WT. Microglia in the primate
1023 macula: specializations in microglial distribution and morphology with retinal position
1024 and with aging. *Brain Struct Funct* **222**, 2759-2771 (2017).

1025

1026 52. Goyal M, Bordt AS, Neitz J, Marshak DW. Trogocytosis of neurons and glial cells by
1027 microglia in a healthy adult macaque retina. *Sci Rep* **13**, 633 (2023).

1028

1029 53. Haverkamp S, Grünert U, Wassle H. The cone pedicle, a complex synapse in the
1030 retina. *Neuron* **27**, 85-95 (2000).

1031

1032 54. Grabner CP*, et al.* Mechanisms of simultaneous linear and nonlinear computations at
1033 the mammalian cone photoreceptor synapse. *Nature communications* **14**, 3486 (2023).

1034

1035 55. Herr S, Ngo IT, Huang TM, Klug K, Sterling P, Schein S. Cone synapses in macaque
1036 fovea: II. Dendrites of OFF midget bipolar cells exhibit Inner Densities similar to their
1037 Outer synaptic Densities in basal contacts with cone terminals. *Visual neuroscience*
1038 **28**, 17-28 (2011).

1039

1040 56. Strettoi E, Raviola E, Dacheux RF. Synaptic connections of the narrow-field, bistratified
1041 rod amacrine cell (AII) in the rabbit retina. *JCompNeurol* **325**, 152-168 (1992).

1042

1043 57. Strettoi E, Masri RA, Grünert U. AII amacrine cells in the primate fovea contribute to
1044 photopic vision. *Sci Rep* **8**, 16429 (2018).

1045

1046 58. Wässle H, Grünert U, Chun MH, Boycott BB. The rod pathway of the macaque monkey
1047 retina: Identification of AII-amacrine cells with antibodies against calretinin.
1048 *JCompNeurol* **361**, 537-551 (1995).

1049

1050 59. Grünert U. Anatomical evidence for rod input to the parvocellular pathway in the visual
1051 system of the primate. *EurJNeurosci* **9**, 617-621 (1997).

1052

1053 60. Hornstein EP, Verweij J, Schnapf JL. Electrical coupling between red and green cones
1054 in primate retina. *Nature neuroscience* **7**, 745-750 (2004).

1055

1056 61. O'Brien JJ, Chen X, Macleish PR, O'Brien J, Massey SC. Photoreceptor coupling
1057 mediated by connexin36 in the primate retina. *J Neurosci* **32**, 4675-4687 (2012).

1058

1059 62. Wool LE, Packer OS, Zaidi Q, Dacey DM. Connectomic identification and three-
1060 dimensional color tuning of S-OFF midget ganglion cells in the primate retina. *J*
1061 *Neurosci* **39**, 7893-7909 (2019).

1062

1063 63. Lamb TD, Simon EJ. The relation between intercellular coupling and electrical noise in
1064 turtle photoreceptors. *J Physiol* **263**, 257-286 (1976).

1065

1066 64. Tessier-Lavigne M, Attwell D. The effect of photoreceptor coupling and synapse
1067 nonlinearity on signal:noise ratio in early visual processing. *Proc R Soc Lond B Biol Sci*
1068 **234**, 171-197 (1988).

1069

1070 65. DeVries SH, Qi X, Smith R, Makous W, Sterling P. Electrical coupling between
1071 mammalian cones. *Current biology : CB* **12**, 1900-1907 (2002).

1072

1073 66. Hsu A, Smith RG, Buchsbaum G, Sterling P. Cost of cone coupling to trichromacy in
1074 primate fovea. *Journal of the Optical Society of America A, Optics, image science, and*
1075 *vision* **17**, 635-640 (2000).

67. Li W, DeVries SH. Separate blue and green cone networks in the mammalian retina. *Nature neuroscience* **7**, 751-756 (2004).

68. Kolb H, Goede P, Roberts S, McDermott R, Gouras P. Uniqueness of the S-cone pedicle in the human retina and consequences for color processing. *JCompNeurol* **386**, 443-460 (1997).

69. Tsukamoto Y, Masarachia P, Schein SJ, Sterling P. Gap junctions between the pedicles of macaque foveal cones. *Vision Res* **32**, 1809-1815 (1992).

70. Hofer H, Carroll J, Neitz J, Neitz M, Williams D. Organization of the human trichromatic cone mosaic. *J Neurosci* **25**, 9669-9679 (2005).

71. Thoreson WB, Mangel SC. Lateral interactions in the outer retina. *Progress in retinal and eye research* **31**, 407-441 (2012).

72. Crook JD, Manookin MB, Packer OS, Dacey DM. Horizontal cell feedback without cone type-selective inhibition mediates "red-green" color opponency in midget ganglion cells of the primate retina. *J Neurosci* **31**, 1762-1772 (2011).

73. Wool LE, Crook JD, Troy JB, Packer OS, Zaidi Q, Dacey DM. Nonselective Wiring Accounts for Red-Green Opponency in Midget Ganglion Cells of the Primate Retina. *J Neurosci* **38**, 1520-1540 (2018).

74. Martin PR, Blessing EM, Buzas P, Szmajda BA, Forte JD. Transmission of colour and acuity signals by parvocellular cells in marmoset monkeys. *J Physiol* **589**, 2795-2812 (2011).

75. Goodchild AK, Chan TL, Grünert U. Horizontal cell connections with short-wavelength-sensitive cones in macaque monkey retina. *Vis Neurosci* **13**, 833-845 (1996).

76. Dacey DM, Lee BB, Stafford DK, Pokorny J, Smith VC. Horizontal cells of the primate retina: cone specificity without spectral opponency. *Science* **271**, 656-659 (1996).

77. Chan TL, Grünert U. Horizontal cell connections with short wavelength-sensitive cones in the retina: A comparison between New World and Old World primates. *JCompNeurol* **393**, 196-209 (1998).

78. Tsukamoto Y, Omi N. Some OFF bipolar cell types make contact with both rods and cones in macaque and mouse retinas. *Frontiers in neuroanatomy* **8**, 105 (2014).

79. Tsukamoto Y, Omi N. OFF bipolar cells in macaque retina: type-specific connectivity in the outer and inner synaptic layers. *Frontiers in neuroanatomy* **9**, 122 (2015).

80. Della Santina L*, et al.* Glutamatergic Monopolar Interneurons Provide a Novel Pathway of Excitation in the Mouse Retina. *Current biology : CB* **26**, 2070-2077 (2016).

81. Lee SC, Weltzien F, Madigan MC, Martin PR, Grünert U. Identification of AII amacrine, displaced amacrine, and bistratified ganglion cell types in human retina with antibodies against calretinin. *J Comp Neurol* **524**, 39-53 (2016).

82. Demb JB, Singer JH. Intrinsic properties and functional circuitry of the AII amacrine cell. *Visual neuroscience* **29**, 51-60 (2012).

83. Diamond JS. Inhibitory Interneurons in the Retina: Types, Circuitry, and Function. *Annu Rev Vis Sci* **3**, 1-24 (2017).

84. Manookin MB, Beaudoin DL, Ernst ZR, Flagel LJ, Demb JB. Disinhibition combines with excitation to extend the operating range of the OFF visual pathway in daylight. *J Neurosci* **28**, 4136-4150 (2008).

1137
1138 85. Wassle H, Puller C, Muller F, Haverkamp S. Cone contacts, mosaics, and territories of
1139 bipolar cells in the mouse retina. *J Neurosci* **29**, 106-117 (2009).
1140
1141 86. Dacey DM, Crook JD, Packer OS. Distinct synaptic mechanisms create parallel S-ON
1142 and S-OFF color opponent pathways in the primate retina. *Visual neuroscience* **31**,
1143 139-151 (2014).
1144
1145 87. Miyagishima KJ, Grünert U, Li W. Processing of S-cone signals in the inner plexiform
1146 layer of the mammalian retina. *Visual neuroscience* **31**, 153-163 (2014).
1147
1148 88. Cowan CS*, et al.* Cell Types of the Human Retina and Its Organoids at Single-Cell
1149 Resolution. *Cell* **182**, 1623-1640 e1634 (2020).
1150
1151 89. Puthussery T, Venkataramani S, Gayet-Primo J, Smith RG, Taylor WR. NaV1.1
1152 channels in axon initial segments of bipolar cells augment input to magnocellular visual
1153 pathways in the primate retina. *J Neurosci* **33**, 16045-16059 (2013).
1154
1155 90. Li J*, et al.* Comprehensive single-cell atlas of the mouse retina. *iScience* **27**, 109916
1156 (2024).
1157
1158 91. Yan W, Laboulaye MA, Tran NM, Whitney IE, Benhar I, Sanes JR. Mouse Retinal Cell
1159 Atlas: Molecular Identification of over Sixty Amacrine Cell Types. *J Neurosci* **40**, 5177-
1160 5195 (2020).
1161
1162 92. Riccitelli S, Vlasits AL, Franke K. Behavior-Specific Computations in the Vertebrate
1163 Retina. *Annu Rev Vis Sci* **11**, 149-173 (2025).
1164
1165 93. Kerschensteiner D. Feature Detection by Retinal Ganglion Cells. *Annu Rev Vis Sci* **8**,
1166 135-169 (2022).

94. Hsiang JC, Shen N, Soto F, Kerschensteiner D. Distributed feature representations of natural stimuli across parallel retinal pathways. *Nature communications* **15**, 1920 (2024).

95. Lennie P, Movshon JA. Coding of color and form in the geniculostriate visual pathway (invited review). *Journal of the Optical Society of America A, Optics, image science, and vision* **22**, 2013-2033 (2005).

96. Crook JD, Packer OS, Troy JB, Dacey DM. Synaptic mechanisms of color and luminance coding: rediscovering the X-Y dichotomy in primate retinal ganglion cells. In: *The New Visual Neurosciences* (eds Chalupa LM, Werner JS). MIT press (2014).

97. Prusky GT, Douglas RM. Characterization of mouse cortical spatial vision. *Vision Res* **44**, 3411-3418 (2004).

98. Lettvin JY, Maturana HR, McCulloch W, Pitts WH. What the frog's eye tells the frog's brain. *Proc IRE* **47**, 1940-1951 (1959).

99. Rucci M, Poletti M. Control and Functions of Fixational Eye Movements. *Annu Rev Vis Sci* **1**, 499-518 (2015).

100. Ko HK, Poletti M, Rucci M. Microsaccades precisely relocate gaze in a high visual acuity task. *Nature neuroscience* **13**, 1549-1553 (2010).

101. Poletti M, Rucci M. A compact field guide to the study of microsaccades: Challenges and functions. *Vision Res* **118**, 83-97 (2016).

102. Shevell SK, Martin PR. Color opponency: tutorial. *Journal of the Optical Society of America A, Optics, image science, and vision* **34**, 1099-1108 (2017).

103. Stockman A, Brainard DH. Color Vision Mechanisms. In: *OSA Handbook of Optics* (ed Bass M). 3rd edn. McGraw-Hill (2010).

104. Lennie P, Haake PW, Williams DR. The design of chromatically opponent receptive fields. In: *Computational models of visual processing* (eds Landy MS, Movshon JA). The MIT Press (1991).

105. Field GD*, et al.* Functional connectivity in the retina at the resolution of photoreceptors. *Nature* **467**, 673-677 (2010).

106. Kim YJ, Packer O, Dacey DM. A circuit motif for color in the human foveal retina. *Proceedings of the National Academy of Sciences of the United States of America* **121**, e2405138121 (2024).

107. Popovych S*, et al.* Petascale pipeline for precise alignment of images from serial section electron microscopy. *Nature communications* **15**, 289 (2024).

108. Lowe DG. Object recognition from local scale-invariant features. In: *Proceedings of the Seventh IEEE International Conference on Computer Vision*). IEEE (1999).

109. Saalfeld S, Fetter R, Cardona A, Tomancak P. Elastic volume reconstruction from series of ultra-thin microscopy sections. *Nature methods* **9**, 717-720 (2012).

110. Consortium TM*, et al.* Functional connectomics spanning multiple areas of mouse visual cortex. *bioRxiv*, 2021.2007.2028.454025 (2023).

111. Lee K, Zung J, Li PH, Jain V, Seung HS. Superhuman accuracy on the SNEMI3D connectomics challenge. *arXiv* **preprint arXiv:1706.00120**, (2017).

112. Lee K, Lu R, Luther K, Seung HS. Learning and Segmenting Dense Voxel Embeddings for 3D Neuron Reconstruction. *IEEE Trans Med Imaging* **40**, 3801-3811 (2021).

113. Macrina T*, et al.* Petascale neural circuit reconstruction: automated methods. *bioRxiv*, 2021.2008.2004.455162 (2021).

114. Dorkenwald S*, et al.* CAVE: Connectome Annotation Versioning Engine. *Nature methods*, (2025).

115. Maitin-Shepard J*, et al.* google/neuroglancer.) (2021).

116. Boycott BB, Wässle H. Morphological classification of bipolar cells of the primate retina. *EurJNeurosci* **3**, 1069-1088 (1991).

117. Wässle H, Boycott BB. Functional architecture of the mammalian retina. *PhysiolRev* **71**, 447-480 (1991).

118. Turner NL, Lee K, Lu R, Wu J, Ih D, Seung HS. Synaptic Partner Assignment Using Attentional Voxel Association Networks. In: *IEEE 17th International Symposium on Biomedical Imaging (ISBI)*) (2020).

119. Lu R, Zlateski A, Seung HS. Large-scale image segmentation based on distributed clustering algorithms. *arXiv* **arXiv.** http://arxiv.org/abs/2106.10795 **[cs.CV]**, 1-8 (2021).